

# 1 Atmospheric Characterization through Fused Mobile Airborne 2 & Surface *In Situ* Surveys: Methane Emissions Quantification 3 from a Producing Oil Field

4 Ira Leifer<sup>1</sup>, Christopher Melton<sup>1</sup>, Marc L. Fischer<sup>2</sup>, Matthew Fladeland<sup>3</sup>, Jason Frash<sup>1</sup>, Warren Gore<sup>3</sup>,  
5 Laura Iraci<sup>3</sup>, Josette Marrero<sup>3</sup>, Ju-Mee Ryoo<sup>3</sup>, Tomoaki Tanaka<sup>3</sup>, Emma Yates<sup>3</sup>

6 <sup>1</sup>Bubbleology Research International, Solvang, CA 93463, [ira.leifer@bubbleology.com](mailto:ira.leifer@bubbleology.com)

7 <sup>2</sup>Lawrence Berkeley National Laboratory, 1 Cyclotron Road, Berkeley CA 94720.

8 <sup>3</sup>NASA Ames Research Center, Moffett Field, CA, 94035

9  
10 **Correspondence to:** Ira Leifer ([Ira.Leifer@bubbleology.com](mailto:Ira.Leifer@bubbleology.com))

11  
12 **Abstract.** Methane (CH<sub>4</sub>) inventory uncertainties are large, requiring robust emission derivation  
13 approaches. We report on a fused airborne/surface data collection approach to derive emissions from an  
14 active oil field near Bakersfield, central California. The approach characterizes the atmosphere from the  
15 surface to above the Planetary Boundary Layer (PBL) and combines downwind trace gas concentration  
16 anomaly (plume) above background with normal winds to derive flux. This approach does not require a  
17 well-mixed PBL, allows explicit, data based, uncertainty evaluation, and was applied to complex  
18 topography and wind flows.

19  
20 *In situ* airborne (collected by AJAX – the Alpha Jet Atmospheric eXperiment) and mobile surface  
21 (collected by AMOG – the AutoMOBILE trace Gas – Surveyor) data were collected on 19 August 2015 to  
22 assess source strength. Data included an AMOG and AJAX intercomparison transect profiling from the  
23 San Joaquin Valley (SJV) floor into the Sierra Nevada Mountains (0.1-2.2 km altitude), validating a novel  
24 surface approach for atmospheric profiling by leveraging topography. The profile intercomparison found  
25 good agreement in multiple parameters for the overlapping altitude range from 500 to 1500 m, for the  
26 upper 5% of surface winds, which accounts for wind-impeding structures, i.e., terrain, trees, buildings,  
27 etc. Annualized emissions from the active oil fields were 31.3±16 Gg methane and 2.4±1.2 Tg carbon  
28 dioxide. Data showed the PBL was not well-mixed at distances of 10-20 km downwind, highlighting the  
29 importance of the experimental design.

## 31 1. Introduction

### 32 1.1. Methane Trends and Uncertainty

33 On decadal timescales, methane (CH<sub>4</sub>), affects the atmospheric radiative balance more strongly than  
34 carbon dioxide (CO<sub>2</sub>), (IPCC, 2007, Fig. 2.21). Since pre-industrial times, CH<sub>4</sub> emissions have risen by a  
35 factor of 2.5 (Dlugokencky et al., 2011; Khalil and Rasmussen, 1995), while estimates of its lifetime has  
36 decreased and now is estimated at ~8.5 years (Sonnemann and Grygalashvily, 2014). Atmospheric CH<sub>4</sub>  
37 growth almost ceased between 1999 and 2006, but has resumed since 2007 (Nisbet et al., 2014;  
38 Schwietzke et al., 2016). Several processes are proposed to underlie this trend (Ghosh et al., 2015; John et  
39 al., 2012) with recent isotopic shifts suggesting wetlands are the dominant driver (Nisbet et al., 2016);  
40 however, high uncertainty in emission inventories (IPCC, 2013) complicates interpretation of the  
41 underlying mechanism(s).

42  
43 The dominant CH<sub>4</sub> loss arises from reaction with hydroxyl (OH), whose concentration has been  
44 increasing in recent decades (John et al., 2012), causing a decrease in the estimated CH<sub>4</sub> lifetime of 0.5%  
45 yr<sup>-1</sup> (Karlsdóttir and Isaksen, 2000). Overall, the estimate of the CH<sub>4</sub> lifetime has decreased by ~40% from  
46 an estimated 12 years in 2007 (IPCC, 2007). Rigby et al. (2017) suggest a decline in OH is likely (66%)  
47 to have contributed to increasing CH<sub>4</sub> since 2007. The recent discovery of a new significant CH<sub>4</sub> loss  
48 mechanism, terrestrial uptake (Fernandez-Cortes et al., 2015), illustrates the need to understand loss  
49 mechanisms better (Allen, 2016).

50  
51 Large CH<sub>4</sub> budget uncertainties remain for many sources (IPCC, 2013) with greater uncertainty in future  
52 trends from global warming feedback (Rigby et al., 2008) and increasing anthropogenic activities  
53 (Kirschke et al., 2013; Saunio et al., 2016; Wunch et al., 2009). Emphasizing these uncertainties are  
54 recent studies that suggest underestimation by a factor of 1.5 in the important anthropogenic CH<sub>4</sub> source,  
55 Fossil Fuel Industrial (FFI) emissions (Brandt et al., 2014). Tellingly, this discrepancy only was noted  
56 recently (Miller et al., 2013), in part because the US CH<sub>4</sub> monitoring network is too sparse to constrain  
57 emissions at “regional to national scales” (Dlugokencky et al., 2013), with isotopic data indicating even  
58 larger underestimation by a factor of 1.6-2.1 (Schwietzke et al., 2016). FFI emissions are the largest  
59 (Brandt et al., 2014; EPA, 2017) or second largest after agriculture (Saunio et al., 2016) anthropogenic  
60 contributor to the global CH<sub>4</sub> budget. These uncertainties strongly argue for the need for new, robust  
61 methodologies for flux derivation.

## 62 1.2. Methane Flux Estimation

63 Various approaches have been developed to derive surface emissions from CH<sub>4</sub> concentration  
64 measurements including direct flux assessment – i.e., measurement of winds and concentrations through a  
65 plane, and/or by the comparison of upwind and downwind mass budgets (Peischl et al., 2016; Peischl et  
66 al., 2015; White et al., 1976), data-driven mass balance, e.g., Karion et al. (2013), tracer-tracer ratio  
67 (LaFranchi et al., 2013), and assimilation inverse models, e.g. Jeong et al. (2013); Jeong et al. (2012);  
68 (Saunio et al., 2017). Challenges for the latter approach include the needs for accurate meteorological  
69 transport models and good *a priori* emission distributions (Miller et al., 2013; Peischl et al., 2016; Smith  
70 et al., 2015). Miller et al. (2013) concluded that bottom-up inventories (EPA, 2013; European  
71 Commission, 2010) significantly underestimate husbandry and FFI emissions. To apportion CH<sub>4</sub> to FFI  
72 versus biological sources, the tracer-tracer approach has been applied using ethane, whose emission ratio  
73 to CH<sub>4</sub> requires tight constraint (Peischl et al., 2013; Simpson et al., 2012; Wennberg et al., 2012). In  
74 practice, this emission ratio is an *a priori* assumption in the assessment.

75

76 Direct assessment approaches have advantages over inversion approaches. Direct approaches allow  
77 explicit uncertainty evaluation and do not require an *a priori* emission spatial distribution, which may be  
78 unknown. Direct approaches also do not require the ability to model atmospheric transport accurately  
79 across the study region. In areas of complex topography or highly variable winds, this transport can  
80 challenge assimilation approaches, which also are challenged in areas with poorly characterized (or  
81 unknown) or highly variable sources, particularly if the measurement network is sparse. For direct  
82 assessment approaches, data collection should be rapid if winds and/or emissions are variable, and at  
83 adequate data density to characterize fine-scale structure.

## 84 1.3. Study Motivation

85 Herein we report on a novel application of fused airborne and surface *in situ* data to directly estimate CH<sub>4</sub>  
86 emissions using an anomaly approach rather than a more typical mass balance approach due to a lateral  
87 gradient in the upwind data. A direct approach does not require accurate winds over the study domain,  
88 only in the measurement plane. The approach was applied to 1164 km of airborne data collected on 19  
89 August 2015 by NASA's Alpha Jet Atmospheric eXperiment (AJAX) while AMOG (AutoMOBILE  
90 greenhouse Gas) Surveyor collected 1074 km of contemporaneous mobile surface data. Both platforms  
91 measure carbon dioxide (CO<sub>2</sub>), CH<sub>4</sub>, water vapor (H<sub>2</sub>O), and ozone (O<sub>3</sub>), as well as winds, pressure,  
92 relative humidity (*RH*), and temperature (*T*). The surface and airborne datasets were collected in a

93 downwind curtain or plane oriented approximately orthogonal to the winds, to characterize the full  
94 planetary boundary layer (PBL) from surface to above the PBL.

95

96 Additionally, the survey route was designed to include an ascent to ~2.2 km above sea level to include  
97 surface PBL characterization. Data fusion between measurement platforms was validated by a vertical  
98 profile intercomparison for 0.5 to 1.5 km altitude by AMOG Surveyor leveraging topographic relief.

#### 99 **1.4 The South San Joaquin Valley, California**

100 Most of California oil production lies in the San Joaquin Valley (SJV), as does most of California  
101 agriculture, including many intensive dairies (Gentner et al., 2014), and the major north-south  
102 transportation artery. For this study, data were collected for the Kern River oil fields (Kern Front oil field,  
103 Kern River oil field and the Poso Creek oil field, referred to herein as the Kern Fields), located adjacent to  
104 northwest Bakersfield (**Fig. 1A**). These adjacent oil fields create a strong CH<sub>4</sub> source that largely is  
105 isolated from confounding plumes from other SJV sources. This area includes complex wind flow  
106 patterns across and around the “toe” of Sierra Nevada Mountain foothills, which extend into the Kern  
107 Front and Kern River oil fields. Here, topographic steering ensures predictable prevailing northwesterly  
108 winds blow across the Kern Fields.

109

110 Strong orographic forcing also arises from tall bluffs (~100 m) on the Kern River Valley’s south bank,  
111 which also separates the Kern River oil field from the urban city of Bakersfield (pop. 364,000 in 2013).  
112 The fine-scale wind structure that results from orographic forcing on transport dictated an anomaly  
113 approach for flux derivation, as did the presence of strong CH<sub>4</sub> structures (plumes) in the valley’s lowest  
114 air. In the anomaly approach, transects must extend beyond a reasonably well-defined plume.

115

116 Topography (i.e., mountain ranges) plays a locally dominant role in overall southern California air flows  
117 where upper level winds locally force the lower level flows that transport pollutants (Bao et al., 2008).  
118 The SJV is delimited on the east by the Sierra Nevada Mountains and on the west by the Transverse  
119 Coastal Mountain Range (**Fig. 1A**). Transport between the SJV and adjacent air basins is poor due to  
120 California’s mountain ranges. The SJV features weak surface winds (Bao et al., 2008) with the worst air  
121 quality in the United States occurring in the cities of Bakersfield and Delano (American Lung  
122 Association, 2016) in the SJV.

123

124 Pacific Ocean air primarily enters the SJV through the San Francisco Bay area and the Carquinez Strait,  
125 where it splits north into the Sacramento Valley and south into the SJV (Zhong et al., 2004). This flow

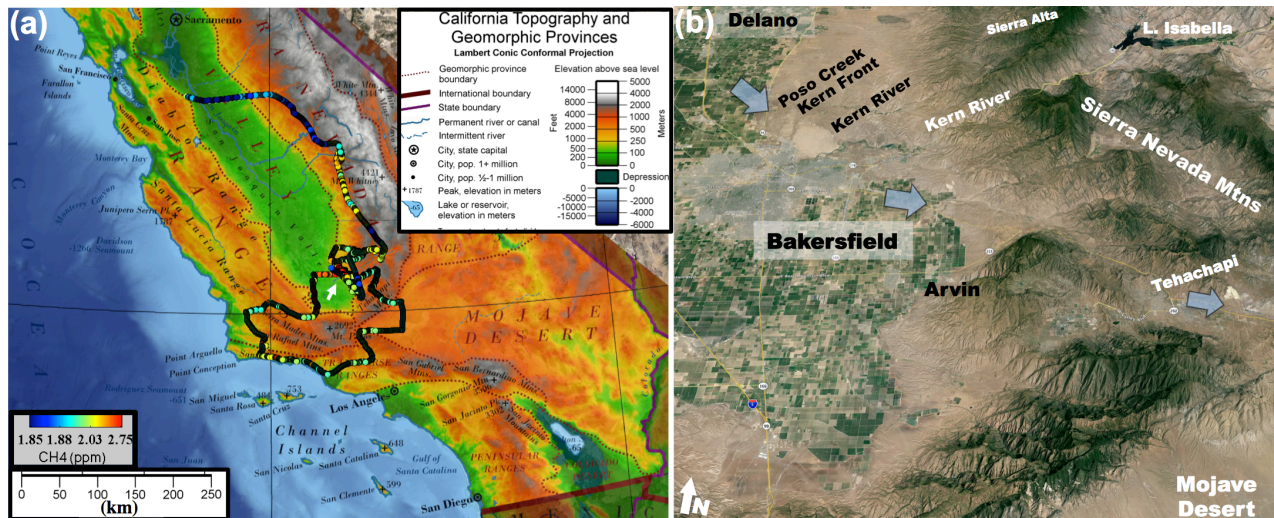


126 extends up to ~1 km altitude (Zhong et al., 2004). These winds are near orthogonal to the 600-km long  
127 central valley of California - i.e., cross-slope. South of Bakersfield, winds shift to from the west due to  
128 mountains that guide SJV air out into the Mojave Desert, where it affects air quality for up to hundreds of  
129 kilometers distance (VanCuren, 2015). Although the Tehachapi Pass is the main exit pathway of SJV air,  
130 other passes also transport air into the Mojave Desert. These flows are augmented by high inland  
131 temperatures relative to the Pacific Ocean, which creates a horizontal pressure gradient that drives local  
132 upslope flows during the day and returning downslope nocturnal flows (Zhong et al., 2004). The pressure  
133 gradient is maximal around sunset, although winds peak ~4 hours later, shortly before midnight. This  
134 pressure gradient is controlled by the semi-permanent Pacific high, situated offshore central California,  
135 which diverts storms far to the north during summer. This pressure feature drives prevailing west-  
136 southwesterly winds at the regional scale in the California south coast air basins (Boucouvala and  
137 Bornstein, 2003).

## 138 **2. Methodology**

### 139 **2.1. Experimental design**

140 Data were collected as part of the *GOSAT-COMEX Experiment* (Greenhouse gases Observing SATellite -  
141 CO<sub>2</sub> and Methane Experiment - GCE) Campaign. GCE was developed to characterize emissions on  
142 spatial scales from decameter (*in situ* surface, imaging spectroscopy) to kilometer (*in situ* airborne) to  
143 deca-kilometer (satellite) in an area of complex topography. GCE design combined *in situ* mobile surface  
144 and airborne data with GOSAT satellite data. *In situ* data serve to assess the satellite pixel / plume  
145 overlap. Key GCE requirements are relatively steady, strong, isolated emissions and predictable and  
146 steady winds. Prevailing study area winds are from the west-northwest, veering to westerly winds to the  
147 southeast of Bakersfield (**Fig. 1**). Prevailing wind directions are highly reliable due to topographic  
148 control.



149  
 150 **Figure 1. (a)** Full surface and airborne data for 19 Aug. 2015 mapped over California topography. White  
 151 arrow shows Bakersfield. Data key on panel. **(b)** Study area map showing direction of daytime prevailing  
 152 winds and nearby mountain topography (Google Earth, 2016). See Supp. Fig. S1 for a high-altitude (20-  
 153 km) photo of the entire study area and surrounding terrain.

154 GCE developed from the COMEX Campaign (Krautwurst et al., 2016), which combined *in situ* airborne  
 155 and surface observations with both imaging and non-imaging spectroscopy to explore synergies for GHG  
 156 emission estimation (Thompson et al., 2015). COMEX focused on southern California CH<sub>4</sub> sources  
 157 including husbandry, landfills, natural geology, and petroleum hydrocarbon refining and production.

158  
 159 GCE combines airborne and surface data collected at dramatically different speeds. AJAX collects data at  
 160 ~500 km hr<sup>-1</sup>, capturing a snapshot of atmospheric winds and plume structure. Surface GCE data are  
 161 collected quasi-Lagrangian, starting northwest (upwind) and proceeding southeast and then east  
 162 (downwind). This enables useful data collection even when a CH<sub>4</sub> plume drifts into the study area after  
 163 the upwind survey – data collection proceeds downwind faster than advection. The surface route was  
 164 designed carefully to traverse all targeted GOSAT pixels using rarely used (low traffic) surface roads and  
 165 requires ~100 minutes.

166  
 167 Airborne and surface surveys are timed so that the downwind data plane (Krings et al., 2011) is surveyed  
 168 concurrent with the satellite overpass. Data planes extend from the surface (AMOG) to above the PBL  
 169 (AJAX), reducing uncertainty by providing a more complete atmospheric characterization including  
 170 below where airplanes are permitted to fly (~500 m in an urban area). AJAX and AMOG profile data are  
 171 fused by an interpolation approach that imposes the observed vertical structure and the flux through the  
 172 data curtain is calculated (Sect. 2.5).

173  
174 GCE first incorporates an AMOG Surveyor upwind transit from Delano (100 m) on the SJV floor to  
175 Sierra Alta (1800 m) and higher to confirm that upwind CH<sub>4</sub> plumes do not threaten to impact the study  
176 area during the experiment, otherwise the survey is aborted. A key mission abort criterion is wind  
177 compliance. Specifically, winds must not be too light (typically less than ~2 m s<sup>-1</sup>) or variable (>30°),  
178 must flush nocturnal accumulations before the GOSAT overpass (i.e., no CH<sub>4</sub> cloud at or nearby upwind  
179 of the site, which means that winds could not have been light as recently as several hours prior; however,  
180 winds are not measured several hours prior), and must be prevailing. The upwind transit provides vertical  
181 profile information including PBL height and vertical structure. AJAX repeats this upwind transect to  
182 compare wind profiles with AMOG; however, discrepancies in the transects arise from the road following  
183 terrain, and the airplane needing to avoid peaks along the ridge.

## 184 **2.2. AutoMOBILE trace Gas (AMOG) Surveyor**

185 Mobile atmospheric surface measurements have been conducted for many years using a customized van  
186 (Lamb et al., 1995) or a recreational vehicle (Farrell et al., 2013; Leifer et al., 2013). Recently, the  
187 development of cavity enhanced absorption spectroscopy (CEAS) analyzers has opened the way for rapid  
188 and highly accurate trace gas measurements (Leen et al., 2013) without the need for onboard compressed  
189 gases as in gas chromatography (Farrell et al., 2013), although periodic calibration with gas standards is  
190 important, albeit typically not onboard the platform. This allows for smaller vehicle survey platforms at  
191 lower logistical overhead (Leifer et al., 2014; McKain et al., 2015; Pétron et al., 2012; Yacovitch et al.,  
192 2015). A competing sensor technology that has been used in mobile survey data collection is open path  
193 spectroscopy (Sun et al., 2014). Mobile survey platforms can incorporate older technology such as  
194 fluorescence to, for example, measure ozone, O<sub>3</sub>.

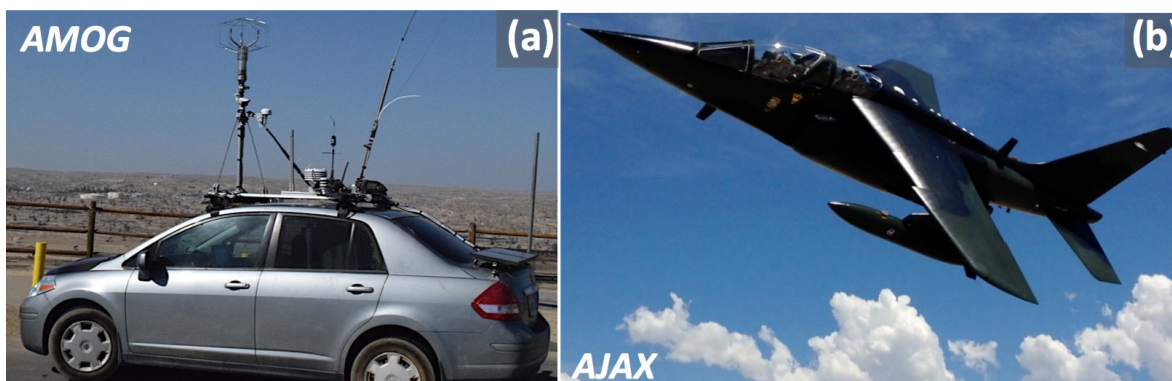
195  
196 Mobile surface data were collected by the AMOG Surveyor (Leifer et al., 2014) (see Supp. Sect. S2.1 for  
197 additional details), a modified commuter car. AMOG Surveyor provides mobile high-speed, high-spatial  
198 resolution observations of meteorology (winds, temperature, pressure), trace gases (greenhouse and  
199 others), and remote sensing parameters. AMOG uses a range of trace gas analyzers and careful design  
200 with respect to wind flow around the vehicle to characterize strong spatial heterogeneity at up to highway  
201 speeds.

202  
203 Two-dimensional winds are measured by a sonic anemometer (VMT700, Vaisala) mounted 1.4 m above  
204 the roof, which is at 1.6 m height, above vehicle flow streamlines for slow to highway speeds. Estimated

205 accuracy is approximately  $10^\circ$  and  $0.3 \text{ m s}^{-1}$  for wind speeds above  $1.5 \text{ m s}^{-1}$  (see supplement for further  
206 details).

207  
208 A high-flow vacuum pump (GVB30, Edwards Vacuum) draws air down a sample lines from 5 and 3 m  
209 above ground for GHG and ozone ( $\text{O}_3$ ) analyzers. The 5-m sample line height references low speed /  
210 stopped ( $< \text{a few m s}^{-1}$ ) AMOG sample collection. At high speed ( $> 10 \text{ m s}^{-1}$ ) the sample tube flexes  
211 backwards to 3 m height to avoid destructively hitting obstacles at high speed. This protects the sample  
212 line from hitting bridges, tree branches, etc. Greenhouse gases,  $\text{CO}_2$ ,  $\text{CH}_4$ , and  $\text{H}_2\text{O}$ , are measured at up to  
213 10 Hz by an Integrated Cavity Offaxis Spectrometer-Cavity Enhanced Absorption Spectroscopy analyzer,  
214 with a 1 s accuracy of 1 ppb for  $\text{CH}_4$  (ICOS-CEAS, 911-0010, Los Gatos Research, Inc.). Calibration is  
215 with a Scott-Marin  $\text{CH}_4$  and  $\text{CO}_2$  atmospheric standard. A fluorescence analyzer measured  $\text{O}_3$  at 0.25 Hz  
216 (49C, ThermoFischer Scientific, MA). This difference does not arise from calibration differences; the  
217 AMOG Surveyor  $\text{O}_3$  analyzer was cross calibrated with the AJAX calibration source to 1 ppb accuracy.  
218 AMOG Surveyor's full trace gas suite (carbonyl sulfide, carbon monoxide, nitric oxide, nitrogen dioxide,  
219 hydrogen sulfide, sulfur dioxide, total sulfur, ammonia) was not deployed on 19 Aug. 2015.

220



221  
222 **Figure 2.** Study platforms. (a) AutoMOBILE trace Gas (AMOG) Surveyor, Kern River oil field in  
223 background. Photo courtesy Ira Leifer. (b) The Alpha Jet Atmospheric eXperiment (AJAX) aircraft, photo  
224 courtesy Akihiko Kuze, JAXA. See Supplemental Material Section 1 for further details.

225  
226 The greenhouse gas analyzer is calibrated using a Scotty's whole-air standard before and/or after each  
227 data collection with the calibration factor closest to the day of flight being applied to each raw  $\text{CO}_2$  and  
228  $\text{CH}_4$  measurement. Calibration factors have been shown to agree within less than 1 ppb. The calibration  
229 factor includes a linear correction for cell pressure, which can drop at higher altitudes. This pressure  
230 calibration has been shown to be linear from 140 mtorr down to 28 mtorr.

231  
232 Relevant recent AMOG Surveyor improvements since Leifer et al. (2014) include a high speed  
233 thermocouple (50416-T, Cooper-Atkins) and a high accuracy (0.2 hPa) pressure sensor (61320V RM  
234 Young Co.). Both are mounted in a roof passive radiation shield (7710, Davis Instruments) to largely  
235 eliminate dynamic pressure effects from the airflow. Position information is critical to accurate wind  
236 measurements and is provided by redundant (two) Global Navigation Satellite Systems (19X HVS,  
237 Garmin) that use the GLONASS, GPS, Galileo, and QZSS satellites at 10 Hz (WGS84). AMOG  
238 analyzers and sensor data are logged asynchronously on a single computer. Custom software integrates  
239 the data streams and provides real-time visualization of multiple parameters in the Google Earth  
240 environment.

### 241 **2.3. Alpha Jet Atmospheric eXperiment (AJAX)**

242 AJAX (Fig. 2b) collected airborne *in situ* measurements of CO<sub>2</sub>, CH<sub>4</sub>, H<sub>2</sub>O by cavity ring down  
243 spectroscopy (G2301-m, Picarro Inc.), O<sub>3</sub>, (Model 205, 2B Technologies Inc.), and meteorological  
244 parameters including 3D winds by the Meteorological Measurement System  
245 (<https://earthscience.arc.nasa.gov/mms>), a NASA developed system with accuracy of  $\pm 1 \text{ m s}^{-1}$ . The  
246 greenhouse gas analyzer is calibrated using NOAA whole-air standards; calibrations are performed before  
247 and/or after each flight with the calibration factor closest to the day of flight being applied to each raw  
248 CO<sub>2</sub> and CH<sub>4</sub> measurement. Further corrections include applying water vapor corrections provided by  
249 Chen et al. (2010) to calculate CO<sub>2</sub> and CH<sub>4</sub> dry mixing ratios. Data also are filtered for quality control for  
250 deviations in instrument cavity pressure, to improve inflight precision.

251  
252 Overall CH<sub>4</sub> measurement uncertainty is typically  $< 2.2 \text{ ppb}$ , including contributions from accuracy of the  
253 standard, precision (1- $\sigma$  over 6 min), calibration repeatability, inflight variance due to cavity pressure  
254 fluctuations, and uncertainty due to water corrections and pressure dependence (based on environmental  
255 chamber studies). See Hamill et al. (2015); Tanaka et al. (2016), and Yates et al. (2013) for further  
256 aircraft and instrumentation details, and Supp. Sect. S2.2.

### 257 **2.4. Background estimation and data fusion**

258 The flux ( $Q(x, z)$ ) in moles  $\text{s}^{-1} \text{ m}^{-2}$  with respect to lateral transect distance ( $x$ ) and altitude ( $z$ ) through the  
259  $x, z$  plane is the product of the normal winds ( $U_N(x, z)$ ) in  $\text{m s}^{-1}$  and the plume concentration anomaly  
260 ( $C'(x, z)$ ) or mole fraction in ppm (Leifer et al., 2016).

$$261 \quad Q(x, z) = k(z) U_N(x, z) C'(x, z) = k(z) U_N(x, z) (C(x, z) - C_B(x, z)) \quad (1)$$

262  $k(z)$  converts from ppm to moles. Interpolation of  $C'$  and  $U_N$  is linear within the PBL and is assumed  
 263 uniform above the PBL. To calculate  $Q(x, z)$  requires  $C'$  relative to background ( $C_B(x, z)$ ). Initially surface  
 264 data that was collected for an upwind surface transect was used to derive  $C_B$ , using the assumption of  
 265 vertical uniformity for “background.”

266  
 267 Unfortunately, the upwind data showed a lateral gradient, which coupled with uncertainty in precisely  
 268 where the downwind air originated (given the topography, which features a gentle incline towards the  
 269 northeast, this gradient is unsurprising, in retrospect). Thus a very small shift in the winds between the  
 270 upwind and downwind curtains results in a significant shift in  $C_B$ , with a very large effect on  $Q$ . As a  
 271 result, the more traditional upwind/downwind mass balance approach was abandoned for an anomaly  
 272 approach.

273  
 274 In the anomaly approach,  $C_B(x, z)$  was derived from evaluating  $C_B(x < x_{max}/2, z)$  and  $C_B(x > x_{max}/2, z)$ ,  
 275 denoted  $C_{BL}(z)$  and  $C_{BR}(z)$ , respectively, where  $x_{max}$  is the lateral extent of the data curtain. Then,  $C_B(x, z)$  is  
 276 derived from a first order linear polynomial fit of  $C_{BL}(z)$  and  $C_{BR}(z)$ .

277  
 278 Both  $C_{BL}(z)$  and  $C_{BR}(z)$  are derived from the amplitude of a Gaussian fit to the left and right probability  
 279 density functions ( $\Phi_L(C(x < x_{max}/2, z))$  and ( $\Phi_R(C(x > x_{max}/2, z))$ ), respectively, for each flight transect level.  
 280 Specifically, for  $\Phi_L$  and  $\Phi_R$ , Gaussian functions are fit to model the plume distribution ( $\Phi_P$ ) and the  
 281 background distribution ( $\Phi_B$ ). In these data,  $\Phi_B$  is well-fit by a single Gaussian, while  $\Phi_P$  is best described  
 282 by multiple Gaussian functions. Then,  $C_{BL}(z)$  and  $C_{BR}(z)$  are defined such that,

$$283 \int \Phi_{BL}(C_{BL}(z)) = 0 \text{ and } \int \Phi_{BR}(C_{BR}(z)) = 0. \quad (2)$$

284 where  $\Phi_{BL}$  and  $\Phi_{BR}$  are the background  $\Phi_B$  for the left and right halves of the data plane, respectively.  
 285 Concentration is not a conserved value, thus  $C'$  is converted into mass ( $N'$ ) by the ideal gas law ( $k$  in Eq  
 286 1) for spatial integration to derive the total emissions ( $E$ ), which is the integration of the flux through the  
 287 plane,  $Q$ ,

$$288 E = \int_{x1}^{x2} \int_0^{z=PBL} Q(x, z) dz dx \quad (3)$$

289 Interpolation, prior to integration, is linear.

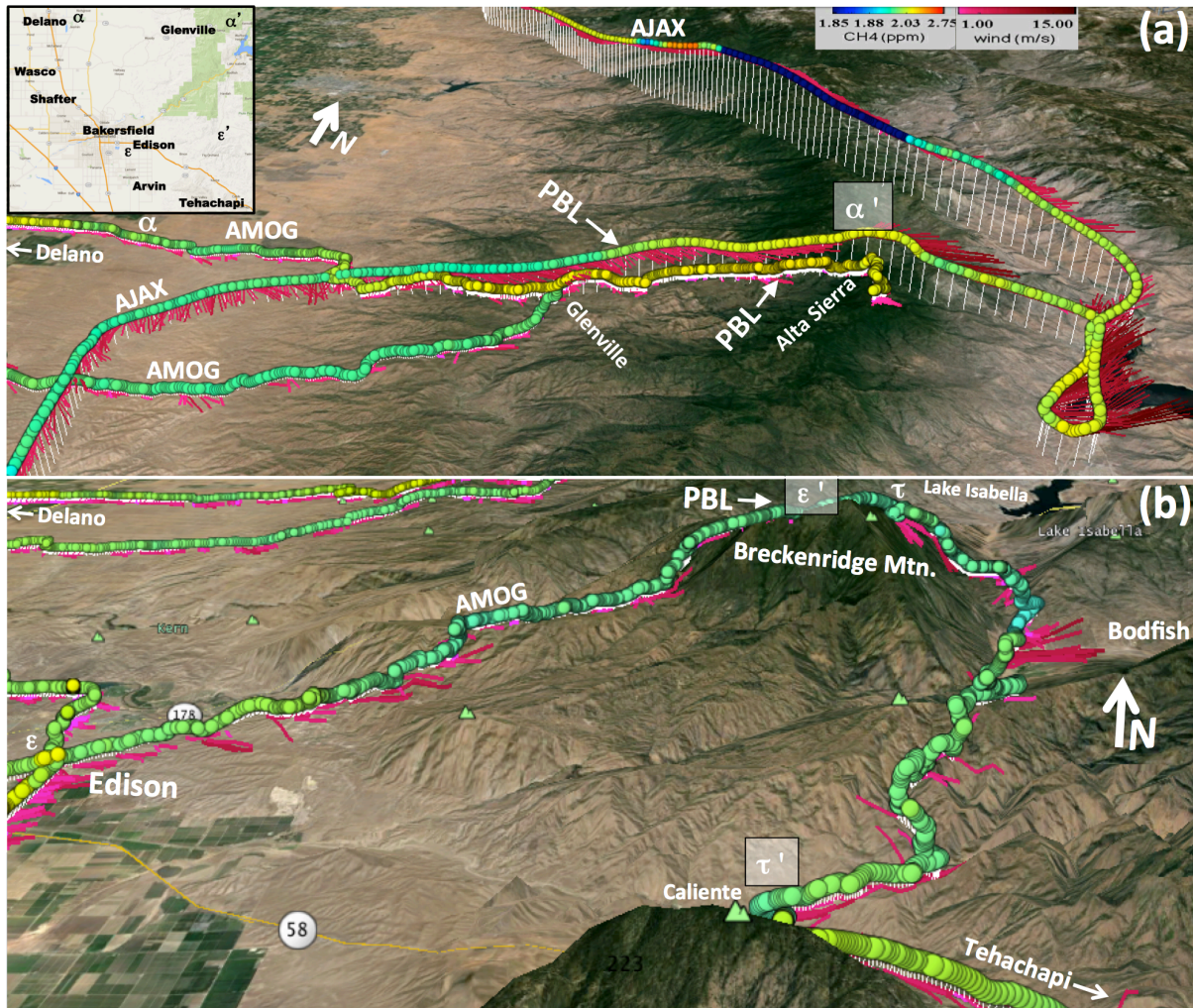
## 290 **2.5. Uncertainty evaluation for emission calculation**

291 A flux estimate requires two types of assumptions with respect to the flux calculation: representativeness  
 292 and representativeness. Specifically, background concentration profiles may be incorrect, while winds,

293 which are measured accurately, could be un-representative, as could concentrations due to temporal  
294 variability over the period needed to make the measurements. Monte Carlo simulations based on observed  
295 data variability were run to assess uncertainty. Instrumental uncertainty is far less than spatial and  
296 temporal variability and hence spatial and temporal variability is the dominant source of uncertainty  
297 (Leifer et al., 2016).

298  
299 Monte Carlo simulations were based on 1 standard deviation in the observed  $U_N(z)$  around the mean for  
300 each flight transect altitude level on the right and left sides, i.e.,  $U_{N_L}(z)$  and  $U_{N_R}(z)$ . Gaussian  
301 distributions with half-widths of  $1\sigma$  based on the values of  $U_{N_L}(x,z)$  and  $U_{N_R}(x,z)$  was formed for each  
302 transect altitude. The distribution was randomly sampled to populate  $U_N(x,z)$ , and then interpolated as  
303 described above. Other variables were Monte Carlo simulated in the same manner - i.e., a Gaussian  
304 distribution was calculated for the left and right portions of the data based on 1 standard deviation in the  
305 observations of the variable around its mean. Variables then were randomly sampled and interpolated.  
306 Specifically, Monte Carlo simulations also addressed  $C_B$ , and  $C$ . Because instrumentation error is so much  
307 less than spatial and temporal variability, Monte Carlo simulation of  $C_b$  represents uncertainty in the  
308 source of the background (upwind) air, which could have some veering from the east or west coupled  
309 with convergence in the horizontal plane. One million Monte Carlo simulations were run for a flux  
310 uncertainty calculation.





311  
 312 **Figure 3.** (a) Pre-survey, upwind AMOG surface and AJAX airborne methane (CH<sub>4</sub>) and winds for  
 313 vertical profile on the Delano – Alta Sierra transect ( $\alpha$ - $\alpha'$ ). Inset shows area map. (b) Post survey,  
 314 downwind AMOG surface profile ascent Edison-Breckenridge ( $\epsilon$ - $\epsilon'$ ) and descent Breckenridge-Bodfish-  
 315 Caliente ( $\tau$ - $\tau'$ ). Upwind profile visible top left. Planetary boundary layer (PBL) identified.

316 **3. Results**

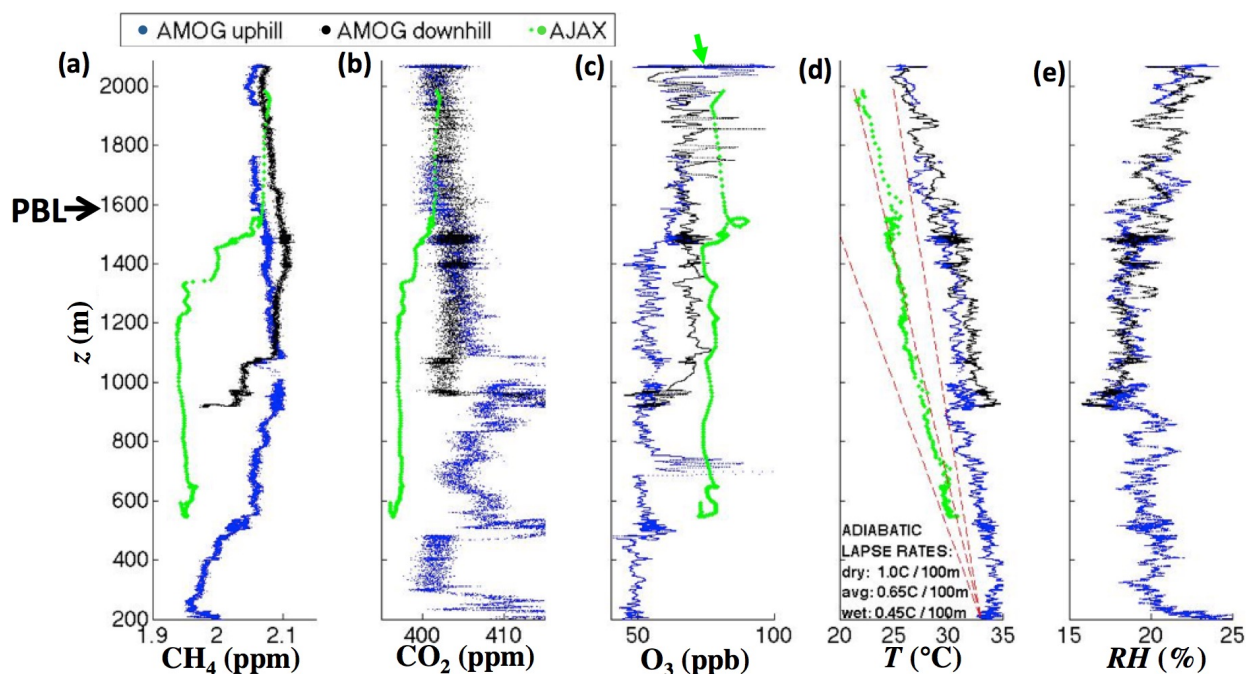
317 **3.1. Profile data**

318 Four vertical profiles (surface and airborne) were collected to understand PBL evolution during the  
 319 survey (2 hrs.) and across the survey domain spanning the experiment. Primary changes were  
 320 development of near surface winds, and a slight increase in the PBL. AMOG and AJAX collected pre-  
 321 survey intercomparison vertical profiles ~30 km north of the Kern Fields between the small town of  
 322 Delano on the SJV floor (100 m) up to a meadow above Shirley Meadows (2058 m) on a ridge of the  
 12



323 Greenhorn Mountains in the Sierra Nevada Mountain Range (Fig. 3). This profile spans a wide range of  
 324 topography, from grasslands on rolling hills, to tall pine trees near Alta Sierra, see Supp. Fig. S5 for  
 325 surface images along the profile. AMOG also conducted a post-survey, downwind vertical atmospheric  
 326 profile to 1800 masl. Approximately 15 minutes of data were collected in an open (200–300 m) field  
 327 above Shirley Meadows (2058 m) that was fairly exposed with only thin stands of pine trees on terrain  
 328 falling steeply off to both sides. The wind direction and speeds for Shirley Meadow was consistent with  
 329 winds at Alta Sierra, several hundred meters below, where AMOG was surrounded by tall trees. Shirley  
 330 Meadows was slightly above the top of the AJAX profile.

331  
 332 The AMOG vertical ascent was collected before the AJAX profile to enable concurrent AMOG/AJAX  
 333 data collection for the Kern Fields. The AMOG ascent/descent was from 18:48 to 21:09 (20:08 UTZ at  
 334 crest), while AJAX flew a descent pattern from 20:58 to 21:04 UTC. The AMOG descent was shortened  
 335 to ~1000 m altitude (Glenville, CA) to allow AMOG to reach the Kern Fields nearly concurrent with  
 336 AJAX and GOSAT.



337  
 338 **Figure 4.** Surface altitude ( $z$ ) above mean sea level profiles for west-east Delano-Alta Sierra transect (Fig.  
 339 3A,  $\alpha$ - $\alpha'$ ) for AMOG and AJAX (a) methane ( $\text{CH}_4$ ), (b) carbon dioxide ( $\text{CO}_2$ ), (c) ozone ( $\text{O}_3$ ), (d)  
 340 temperature ( $T$ ), and (e) relative humidity ( $RH$ ). Also shown on (d) are the dry, average, and wet adiabatic  
 341 lapse rates. Data key on panel, planetary boundary layer (PBL), labeled. Green arrow shows extrapolation  
 342 of AJAX trend to Shirley Meadows altitude (2058 m).

343 Overlapping AMOG and AJAX profile data were collected between 500 and 2000 m. There was very  
344 good agreement between the two platforms for CO<sub>2</sub> and CH<sub>4</sub> for altitudes between 1.55 and 2 km (Fig. 4a  
345 and 4b), 99.9% and 99.7%. AMOG and AJAX CH<sub>4</sub> concentrations decreased notably from the well-  
346 mixed PBL to the near surface layer, from ~2.07 ppm (500-750 m) to ~1.93 ppm (250-300 m). AJAX also  
347 showed a decrease in CO<sub>2</sub> from 403 ppm to below 400 ppm. The CO<sub>2</sub> decrease was consistent with a  
348 shift to agricultural air where CO<sub>2</sub> vegetative uptake reduces CO<sub>2</sub> concentrations. The PBL grew from  
349 600 to 900 m between AMOG's ascent and descent and then to 1500 m by the time of AJAX's descent  
350 based on the CH<sub>4</sub>, CO<sub>2</sub>, and O<sub>3</sub> data.

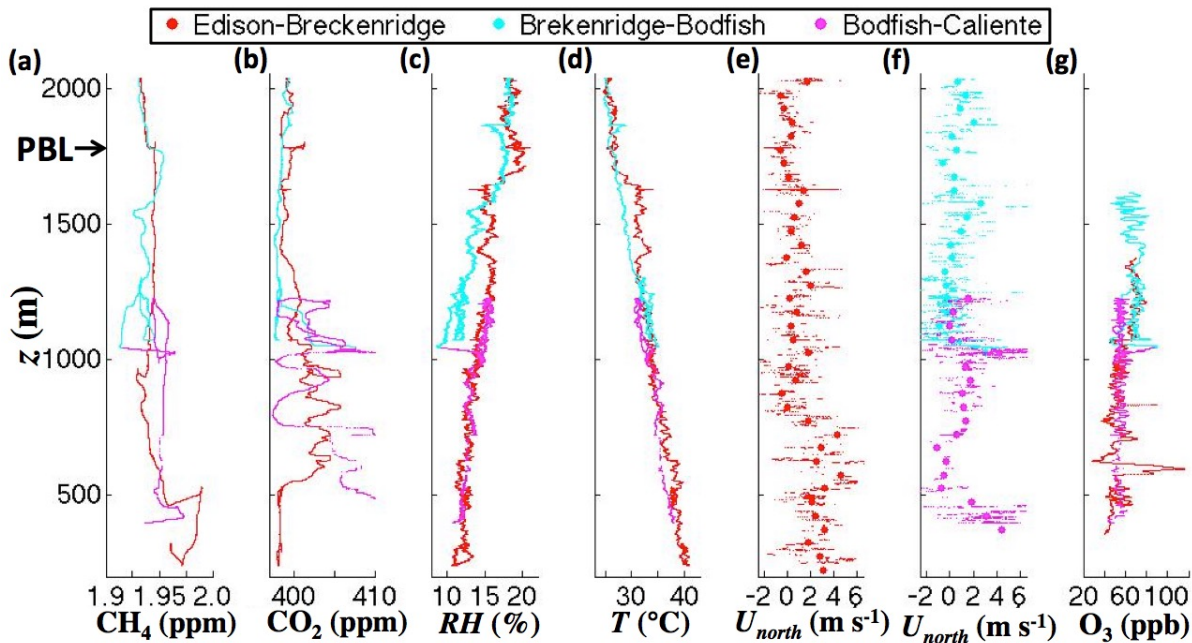
351  
352 The PBL was identified at ~1580-1600 m based on both surface and airborne relative humidity (*RH*) and  
353 temperature (*T*) vertical profiles. Winds were not useful for deriving the location of the PBL. Diurnal  
354 heating is apparent between the two AMOG Surveyor *T* profiles, but does not change the lapse rate.  
355 Because AJAX flies above the surface where AMOG collects data, AJAX temperatures are lower. In the  
356 lower atmosphere, the lapse rate was 6.9°C km<sup>-1</sup> for AJAX between 500-900 m, while the AMOG lapse  
357 rate from 200-900 m was a similar 5.6°C km<sup>-1</sup>. Between 950 and the top of the PBL, AMOG lapse rates  
358 were much shallower, 2.5 °C km<sup>-1</sup>, with a jump in temperature at 900 m. Above the PBL, the AMOG  
359 lapse rate was 3.5°C km<sup>-1</sup>, close to the wet adiabatic lapse rate (Fig. 4d).

360  
361 Above the PBL, O<sub>3</sub> concentrations between AMOG and AJAX were ~20 ppb different although the  
362 AMOG and AJAX profile slope (dO<sub>3</sub>/dz) were the same. If the trend in AJAX O<sub>3</sub>(z) from 1600 to 1850 m  
363 is extended to z = 2058 m (Fig. 3C, green arrow), there is agreement with AMOG Shirley Meadows (open  
364 field) O<sub>3</sub> concentrations. This similar slope but different absolute value could indicate O<sub>3</sub> loss as it  
365 diffused down through the pine canopy to the surface (and AMOG). Tall pine trees (30+ m) dominate  
366 above ~1700, except for Shirley Meadows where, as noted, there was good agreement. For 900 < z <  
367 1400 m, AJAX - AMOG agreement was better for the descent, which was closer in time to AJAX than  
368 the ascent. This shift likely was associated with formation of the daytime PBL.

369  
370 In this upwind profile, AJAX observed elevated O<sub>3</sub> that was well mixed down to 500 m, while earlier  
371 AMOG showed well-mixed O<sub>3</sub> down to only 1100 m. There also was a small (~10 ppb) O<sub>3</sub> enhancement  
372 at the top of the PBL in both the airborne and surface profiles. The highest O<sub>3</sub> concentrations were  
373 observed by AMOG in Shirley Meadows, where visibility was low due to smoke aerosols from the Rough  
374 Fire (NASA, 2015). Air above the PBL was more humid than elsewhere in the profile, except for the  
375 lowest 50 m above the valley floor, which was enriched in CH<sub>4</sub>, CO<sub>2</sub>, and *RH*, possibly from nocturnal  
376 accumulation and agriculture including irrigation *RH* inputs. There were thin, atmospheric layers that

377 suggest remnant structures from the prior day. For example, at  $\sim 550$  m the air changed character, with a  
 378 jump in  $\text{CO}_2$  by  $\sim 10$  ppm, and of  $\text{O}_3$  by  $\sim 10$  ppb, and a decrease in the  $\text{CH}_4$  altitude gradient ( $d\text{CH}_4/dz$ ).

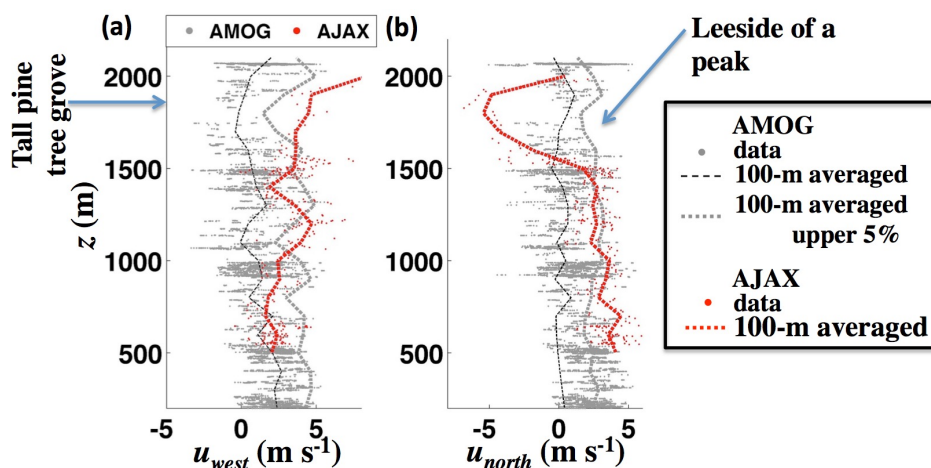
379  
 380 Air was more polluted at greater altitude above the PBL in the upwind (Delano – Alta Sierra) profile for  
 381  $\text{O}_3$  for both platforms with air 10-20 ppb greater than in the PBL. Additionally, AJAX  $\text{CH}_4$  and  $\text{CO}_2$  were  
 382 significantly higher above the PBL. The AMOG  $\text{CH}_4$  and  $\text{CO}_2$  data are less clear, presumably because  
 383 AMOG data were prior to the disappearance of the nocturnal, stably stratified PBL. This was consistent  
 384 with visual observations of haze by AMOG from Shirley Meadows as well as by the AJAX pilot. Also,  
 385 air above the PBL was more humid.



386  
 387 **Figure 5.** Surface altitude ( $z$ ) above sea level profiles for Edison-Breckenridge ascent (red) and descent  
 388 (blue) to Bodfish and then Caliente profile (magenta) (Fig. 3b) for AMOG Surveyor (a) methane ( $\text{CH}_4$ ),  
 389 (b) carbon dioxide ( $\text{CO}_2$ ), (c) relative humidity ( $RH$ ), (d) temperature ( $T$ ), north wind ( $U_{north}$ ), for (e)  
 390 ascent and (f) descent, dots shown 50-m altitude binned averaged, and (g) ozone ( $\text{O}_3$ ). Planetary  
 391 Boundary Layer (PBL) labeled.

392  
 393 A downwind ascent profile in the SJV was collected from Edison, CA to the high flanks of Breckenridge  
 394 Mountain, followed by a descent behind the Breckenridge Mountain to Caliente, CA through the tiny  
 395 town of Bodfish (Fig. 3b). This descent was separated from the SJV by a ridge and includes dryer, clean  
 396 air is that is representative of air from around Lake Isabella, a fairly isolated mountain valley. The  
 397 downwind profile was collected quasi-Lagrangian in that the time separating the two profiles (about four

398 hours) is comparable to the transport time (75 km at a mean wind speed of  $4 \text{ m s}^{-1}$ , implies 5 hours for  
 399 transport). Thus, the downwind profile was for close to the same air. Over these hours, there was some  
 400 additional PBL development,  $\sim 100 \text{ m}$  growth to  $\sim 1675 \text{ m}$ , with highly uniform  $\text{CH}_4$  between 1000 m and  
 401 the top of the PBL (Fig. 5a). Thus, the PBL remained fairly stable over the course of the study. Air in  
 402 both the upper PBL and above was cleaner with lower humidity and  $\text{CH}_4$  concentrations. Unfortunately,  
 403 the  $\text{O}_3$  analyzer overheated during the ascent and resumed collecting data on the descent at  $\sim 1500 \text{ m}$ .



404  
 405 **Figure 6.** Altitude ( $z$ ) profiles for (a) west (upslope) and (b) north (cross slope) wind components from  
 406 AMOG and AJAX for overlapping altitudes of the Delano–Alta Sierra transit (Fig. 3,  $\alpha$ – $\alpha'$ ), 100-m  
 407 altitude rolling-averaged data for AJAX, AMOG, and AMOG upper 5% of winds. Data key on figure.

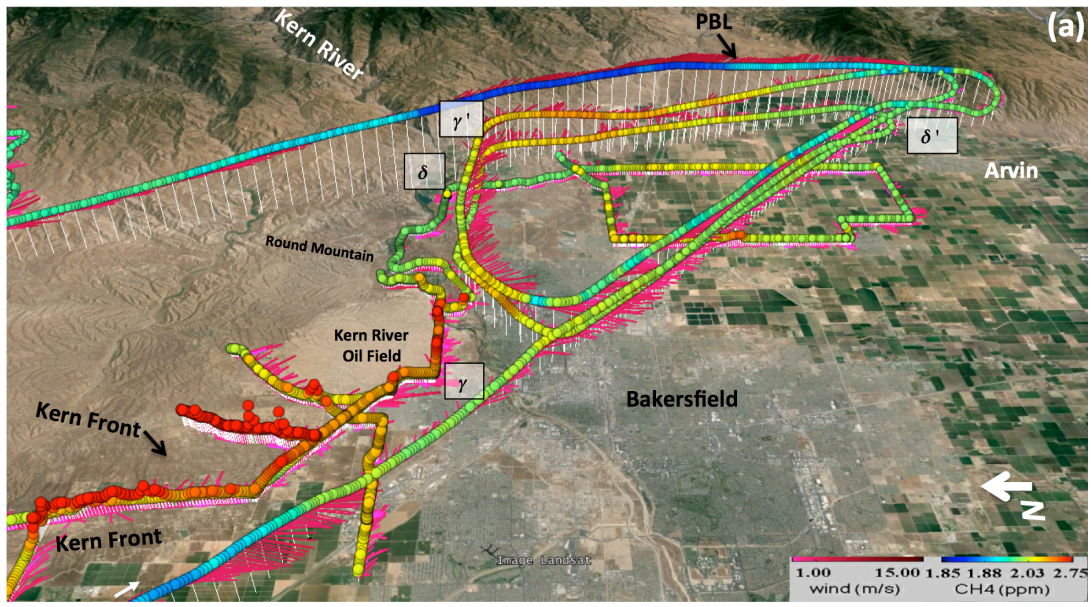
408  
 409 Direct comparison between AMOG and AJAX winds is inappropriate because AMOG winds are affected  
 410 strongly by obstacles including hills, trees, and buildings. However, in many instances, terrain is open, or  
 411 gently rolling hills, and there tend to be regions of stronger winds that we propose are representative of  
 412 free atmosphere winds. AMOG data were altitude binned and the strongest winds in each bin were  
 413 compared with AJAX (Fig. 6). Agreement is generally good (within 15-20%) between the upper 5% of  
 414 AMOG cross-slope (west) winds in each altitude-averaged band (Fig. 6a). For the upslope wind (north)  
 415 agreement is better (within 5-10%) for a larger range of altitudes (Fig. 6b). This allows fusions of the  
 416 upper 5% of AMOG winds with AJAX winds. Over the full altitude range, the median differences were  
 417 38% and 27% for the north and east wind components. The altitude variation in the agreement is shown in  
 418 Supp. Fig. S7.

## 419 **3.2. Kern Fields and Bakersfield Greenhouse Gas Emissions**

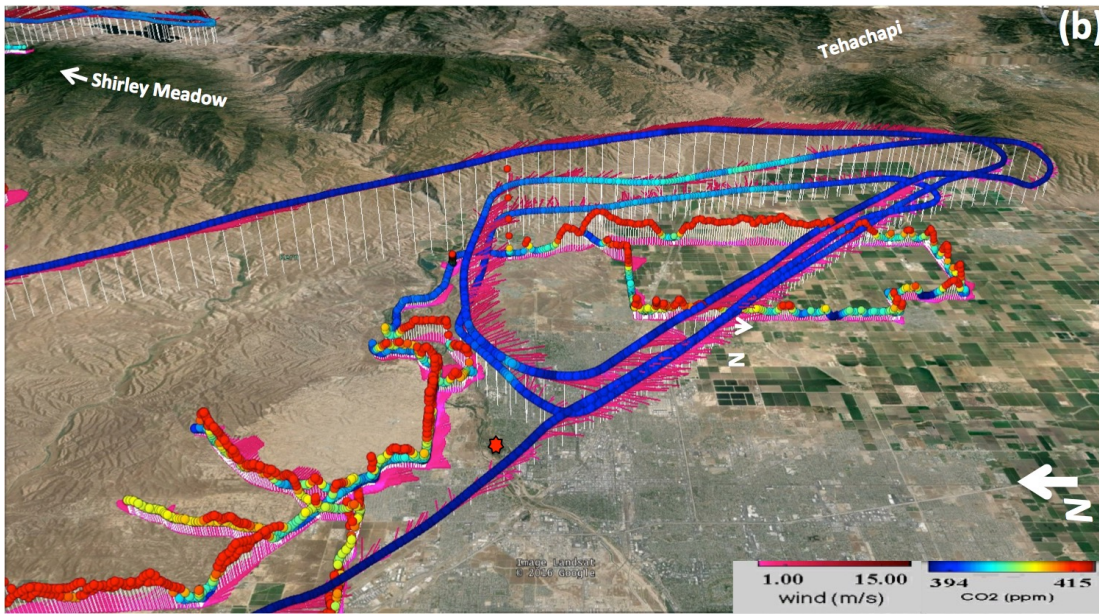
### 420 **3.2.1 Methane**

421 On 19 Aug. 2015, winds over the Kern Fields were prevailing (northwesterly) and fairly strong ( $\sim 3 \text{ m s}^{-1}$ )  
422 on the ground and somewhat stronger aloft (Fig. 7). Potential plumes from the only nearby upwind dairy  
423 (Fig. 7a, white arrow) were directed by winds to pass to the west of the oil fields, agricultural fields in this  
424 part of the SJZ are dry. As a result, surface topography like the Kern River Bluffs imposed only small  
425 wind modification at the surface and at altitude. Southeast of Bakersfield, winds veered to westerlies  
426 towards passes in the Sierra Nevada Mountains that connect to the Mojave Desert. The downwind survey  
427 included two plume transits on agricultural roads with negligible to no traffic. These transits clearly  
428 showed the plume's eastward drift, passing to the north of the small town of Arvin, CA.



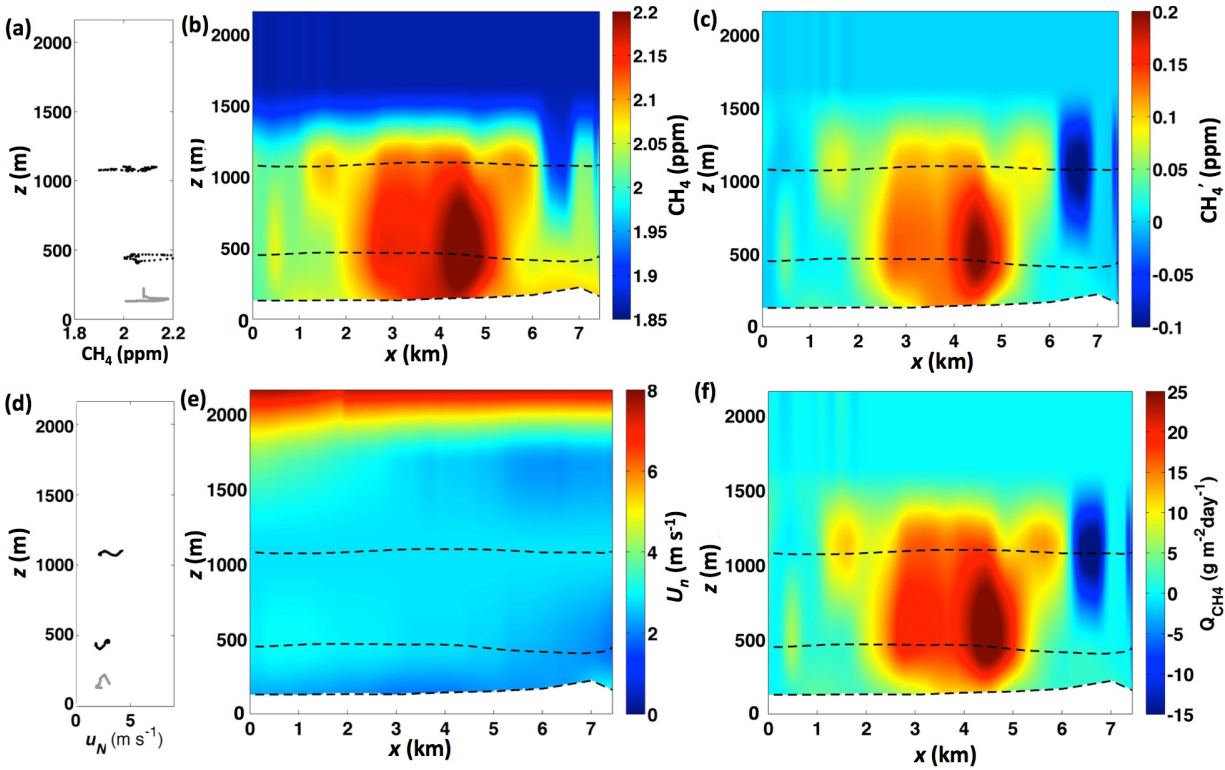


429



430

431 **Figure 7.** Combined AJAX and AMOG winds and *in situ* (a) methane (CH<sub>4</sub>) and (b) carbon dioxide  
 432 (CO<sub>2</sub>) for the Kern Fields on 19 Aug. 2015 for prevailing wind conditions. White arrow to the west of  
 433 Kern Front oil field shows location of nearby dairy. Greek letters identify two downwind curtains. Red  
 434 star on (b) locates origin for transect  $\gamma$ - $\gamma'$ . Data keys on figure.



435  
 436 **Figure 8.** (a) Methane (CH<sub>4</sub>) altitude ( $z$ ) profiles for 19 Aug. 2015 for AJAX (black) and AMOG (gray)  
 437 data. (b) Interpolated, fused AJAX and AMOG CH<sub>4</sub> data, with respect to lateral east distance ( $x$ ) relative  
 438 to 119.0023°W, 35.3842°N for data plane  $\gamma$ - $\gamma'$  (Fig. 7). Dashed lines show data locations. (c) CH<sub>4</sub>  
 439 anomaly (CH<sub>4</sub>') relative to the background data plane (Supp. Fig. S6A). (d) Vertical normal wind profile  
 440 ( $U_n$ ) from AJAX (black) and AMOG (gray) data during ascent/descent, (e) interpolated, fused  $U_n$ , and (f)  
 441 CH<sub>4</sub> flux ( $Q_{CH_4}$ ) for the Kern Fields. Data key on panels.

442  
 443 The background CH<sub>4</sub> plane  $C_B(x,z)$  was extracted from the CH<sub>4</sub> data outside the plume –  $C_{BL}(z)$  and  
 444  $C_{BR}(z)$ , see Eqn. (2) – immediately downwind of the Kern Fields (transect  $\gamma$ - $\gamma'$ ).  $C_B$  showed a slight  
 445 increase towards the east of ~20 ppb (Supp. Fig. S6a). The normal wind ( $U_n$ ) was fairly uniform across  
 446 the data plane, including downwind of the canyon (Fig. 8e). Thus, the CH<sub>4</sub> flux ( $Q_{CH_4}(x, z)$ ) shows similar  
 447 spatial patterns to CH<sub>4</sub>'( $x, z$ ). Emissions from the Kern Fields' were dominated by a large, focused CH<sub>4</sub>  
 448 plume (or group of plumes) in the core of a much broader, dispersed, and poorly defined plume. This  
 449 structure is evident in both surface AMOG data and in the lowest AJAX altitude for plane  $\gamma$ - $\gamma'$  with both  
 450 showing the strongest peak at  $x = 4.5$  km (Fig. 8b, dashed lines). Total estimated emissions ( $E$ ) were  
 451  $63.5 \pm 50\%$  Mol s<sup>-1</sup> (equivalent to 32 Gg yr<sup>-1</sup>). Uncertainty is from the Monte Carlo simulations, described  
 452 in section 2.5.

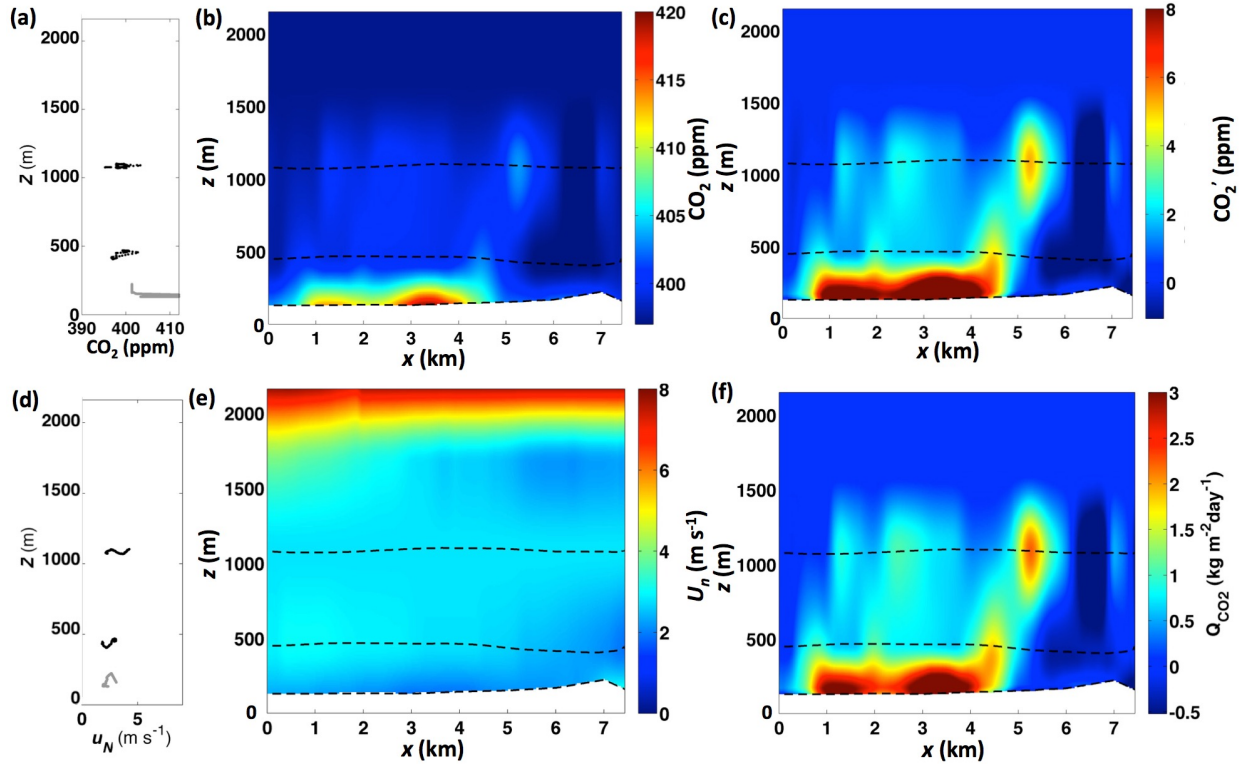
453  
454 Within the plume, concentrations are elevated at 1200 m altitude relative to 500 m and the surface,  
455 indicating buoyant rise. Additional evidence for buoyant rise is provided by two small plumes at  $x \sim 1.7$   
456 and 5.7 km were centered at the top of the PBL but were not also observed in surface and mid altitude  
457 data. The upper AJAX flight line was several hundred meters below the top of the PBL (at  $\sim 1580$  m, Fig.  
458 4), which constrains the main plume and was centered vertically in the PBL. Concentrations above the  
459 PBL were determined from AJAX descent and ascent data (Fig. 4), in agreement with AMOG data above  
460 the PBL. These observations show that the plume was not well mixed across the PBL. Another important  
461 feature is the upper altitude clean air intrusion at  $x \sim 6.5$  km lies downwind of Round Mountain Canyon to  
462 the east of the Kern River oil field (Fig. 8b, Fig. 7a for location). This intrusion does not penetrate down  
463 to 500 m and represents a downslope airflow of cleaner upper level air.

464  
465 For comparison, a recent bottom-up estimate of  $\text{CH}_4$  emissions based on production data for the Kern  
466 Fields estimated  $10\text{-}40 \text{ Gg CH}_4 \text{ yr}^{-1}$  (68% Confidence Level), by combining oil and gas production data  
467 with US-EPA emissions factors for associated wells (Jeong et al., 2014). Other  $\text{CH}_4$  sources are unlikely  
468 to confuse this interpretation as petroleum system emissions are  $\sim 20$  times larger than estimated nearby  
469 livestock and landfill  $\text{CH}_4$  emissions of  $\sim 2.3$  and  $1.4 \text{ Gg yr}^{-1}$ , respectively (Calgem, 2014).

### 470 **3.2.2. Carbon Dioxide**

471 Background  $\text{CO}_2$  for data curtain  $\gamma\text{-}\gamma'$  (Supp. Fig. S6b) was highly uniform. Given the strong crosswinds  
472 and care taken to avoid trailing other vehicles on the low-trafficked China Loop Road, these data passed  
473 quality review— $\text{CO}_2$  exhaust contamination manifests as a dramatic increase in the standard deviation as  
474 AMOG intersects a turbulent vehicle exhaust plume. There was a shallow  $\text{CO}_2$  layer constrained to the  
475 lower 100 to 200 m with  $\sim 10$  ppm enhancement (Fig. 9a), also observed in the  $\text{CO}_2$  vertical profile (Fig.  
476 4b), a layer that was characterized by elevated relative humidity. Further evidence that these broad spatial  
477  $\text{CO}_2$  emissions are real is from the spatial similarity to  $\text{CO}_2$  enhancements in the lowest AJAX flight data  
478 (Fig. 9c). For example the surface  $\text{CO}_2$  plume was strongest at  $x \sim 4.5$  km in AMOG and AJAX data. The  
479 broad spatial extent of these emissions, similar to the broad  $\text{CH}_4$  emissions suggests a relationship to  
480 field-scale (engineering or geological) processes. Overall  $\text{CO}_2$  emissions were  $1730 \pm 50\% \text{ Mol s}^{-1}$   
481 (equivalent to  $2.4 \pm 1.2 \text{ Tg yr}^{-1}$ ).





482

483 **Figure 9.** (a) Vertical carbon dioxide (CO<sub>2</sub>) altitude ( $z$ ) profile data for 19 Aug. 2015 for AJAX (black)  
 484 and AMOG (gray) data. (b) Interpolated, fused AJAX and AMOG CO<sub>2</sub> data curtain with respect to lateral  
 485 east distance,  $x$ , relative to 119.0023°W, 35.3842°N for curtain  $\gamma$ - $\gamma'$  (Fig. 7b). Dashed lines show data  
 486 locations. (c) CO<sub>2</sub> anomaly (CO<sub>2</sub>'). (e) Vertical normal wind profile ( $U_n$ ). (e) Interpolated, fused  $U_n$ , and  
 487 (f) CO<sub>2</sub> flux ( $Q_{CO2}$ ) for the Kern River and Kern Front oil fields for 19 Aug. 2015. Data key on panels.

488 There was a strong CO<sub>2</sub> anomaly in a focused plume at  $x = 5$  km and  $z = 1$  km. This plume likely relates  
 489 to the two cogeneration power plants located in the Kern River oil field. Further support for this  
 490 interpretation is its co-location with a similarly focused CH<sub>4</sub> plume at the same location. This power  
 491 plant-related feature is a persistent feature that has been observed in other surveys (Leifer – unpublished  
 492 data). The upper clean air intrusion in the CH<sub>4</sub> data curtain also is apparent in the CO<sub>2</sub> data (Fig. 9b), in  
 493 front of Round Mountain Canyon (Fig. 7).

494

495 Based on a reservoir CO<sub>2</sub>:CH<sub>4</sub> gas ratio of 92.2%:1.7% (Lillis et al., 2008) and 32 Gg yr<sup>-1</sup> CH<sub>4</sub> emissions,  
 496 the Kern Fields' CO<sub>2</sub> emissions were predicted to be 1.8 Tg yr<sup>-1</sup>, which is fairly consistent with the  
 497 directly derived emissions of 2.4 Tg yr<sup>-1</sup>. Both these values are somewhat lower than the inventory for the  
 498 cogeneration plants in Kern River oil field, 3.1 Tg yr<sup>-1</sup> (CARB, 2016). The disagreement with inventory  
 499 likely arises from the co-generation plant only being active some of the time, confirmed by data from the  
 500 GOSAT-COMEX campaign.

501

502 **4. Discussion**

503 **4.1. Experimental design and real-time visualization**

504 Ideally, GCE airborne and surface data are collected first upwind and then downwind. However, AJAX  
505 airborne data are not collected in a Lagrangian sense as would be necessary for slower, less maneuverable  
506 airborne platform thanks to its extreme speed and maneuverability. This allows collection of near  
507 snapshot (~30 minutes) data. Slower, AMOG surface data were collected in a quasi-Lagrangian sense,  
508 reducing the likelihood of confounding interference in the study area from non-FFI SJV inputs due to  
509 wind shifts after the pre-survey (for non-nominal winds the collection is aborted). Given the AJAX-  
510 AMOG speed difference, concurrent surface and airborne data could not be collected both upwind and  
511 downwind, and thus, concurrency was prioritized for downwind. For flight efficiency and to provide  
512 downwind concurrency with AMOG, AJAX flew a triangle that allowed AJAX to complete transects at  
513 three altitudes in close to AMOG's upwind-downwind survey time.

514  
515 After the Kern Fields survey, AJAX returned to base, while AMOG collected additional surface data,  
516 exploring the fate of emissions from the Kern Fields. The word, "exploring" is significant, as real-time  
517 visualization of winds, CH<sub>4</sub>, and O<sub>3</sub> guided the downwind surveying. Data were collected to test the  
518 hypothesis that there was a relationship between wind strength and the specific outflow path from the SJV  
519 to Mojave Desert - specifically, that more northerly passes, which require greater wind veering from  
520 prevailing are preferred at lower winds speeds. The AMOG survey first confirmed that outflow was not  
521 up the Kern River Valley, and then collected a downwind vertical profile into the Sierra Nevada  
522 Mountains to search for outflow through a pass near Breckenridge Mountain. After confirming its  
523 absence, AMOG then investigated in the Tehachapi Pass, where the outflow was identified. Thus, on 19  
524 Aug. 2015, when winds were strong, the outflow was by the most direct pathway - the Tehachapi Pass.

525 **4.2. Experimental design and uncertainty reduction**

526 The experimental design reduced uncertainty by characterizing the PBL through surface and airborne data  
527 fusion so that a well-mixed PBL is not required. Note, for a well-mixed PBL, surface-airborne data fusion  
528 does not reduce uncertainty. The benefit arises for a not well-mixed PBL where a significant fraction of  
529 the plume mass lies below the lowest altitude the airplane can fly. In such case, surface data inclusion

530 adds information to the PBL characterization. For example, flights are often face airspace restrictions for  
531 a number of conditions including cities, approach pathways, military airspace, and/or safety.

532 Aerial survey altitudes were designed to span from near the top of the PBL to as low as permissible and  
533 an intermediate level (0.5, 1, 1.2 km). Thus, surface data added information on the lowest third of the 1.6-  
534 km thick PBL. This lower portion of the PBL is more important on days when the PBL is shallower.

535 Observations showed that the well-mixed PBL assumption was poor as far as 10-20 km downwind. One  
536 solution is to collect data even further downwind, where the PBL should be better mixed (White et al.,  
537 1976); however, secondary (potentially uncharacterized) sources downwind of the study area and upwind  
538 of the downwind data plane add confounding anomalies. Also, wind flow complexity can lead to transport  
539 orthogonal to the overall downwind direction, leading to flux leakage out of the plume. The likelihood of  
540 plume loss increases over greater distances. And finally, as the PBL evolves with time, it imposes an  
541 evolving structure on the wind and concentration vertical profiles, which also challenge the well-mixed  
542 PBL assumption – particularly if transport to the downwind plane requires hours.

543  
544 The *in situ* analyzers record concentration and winds with very high accuracy; however, only at a single  
545 location and time. Thus, *in situ* uncertainty arises mostly from inadequate characterization of temporal  
546 variability and spatial heterogeneity in winds and emissions over the survey time period. The best strategy  
547 is to minimize study time; however, there is a necessary tradeoff between spatial resolution and study  
548 time. AJAX collects data quickly, allowing survey completion within far less than typical atmospheric  
549 change timescales. Similarly, the surface survey route was designed to minimize collection time,  
550 primarily on rural/agricultural roads carefully selected to avoid traffic congestion and traffic lights. The  
551 surface survey requires ~90 minutes to complete and is conducted quasi-Lagrangian.

552  
553 GCE treats uncertainty explicitly, allowing improvements in the data collection strategy to reduce  
554 uncertainty. For example, the east-west downwind transect was lengthened from earlier data collects to  
555 characterize background concentrations better. GCE also does not require an *a priori* emission  
556 distribution and thus incorporates explicitly emissions from super-emitters, normal emitters, and  
557 distributed sources, improving robustness of the findings. In contrast, inversion models require a  
558 reasonable spatial *a priori* emission distribution and the ability to model transport across the study  
559 domain. However, complex wind flows from fine-scale topographic structures, as observed for the Kern  
560 Fields, challenge transport modeling.

561 **4.3. Profile intercomparison**

562 This study leveraged terrain to provide profile information with a surface mobile platform, which was  
563 compared with airborne data. In this study, the two were combined to provide more complete coverage of  
564 the atmosphere than a single platform could, at a fraction of the cost (not to mention logistical  
565 complexity) of having two airborne platforms. Whereas the approach worked well in the San Joaquin  
566 Valley, further research is needed to confirm its utility in other settings.

567  
568 Above the PBL, there was excellent agreement between surface and airborne concentration profile data,  
569 while concentration profiles within the PBL show significant differences between the two profiles, likely  
570 related to air mass shifts and diurnal heating during the time between the profiles (Fig. 4). Winds above  
571 the PBL were in poor agreement, with the north component in the opposite direction (Fig. 6). Underlying  
572 this discrepancy was a mountain peak, which clearly caused large-scale alterations in the wind flow field.

573  
574 Within the PBL, agreement between unfiltered surface AMOG winds and AJAX winds was poor,  
575 unsurprising because surface winds are strongly affected by obstacles. However, by filtering AMOG  
576 winds (collected 3-m above the surface) for the strongest 5%, agreement was within 15-20% for the  
577 along-slope – i.e., north – winds, and better for upslope winds (west). Specific exceptions were when  
578 AMOG was in a dense grove of pines, and when AJAX flew behind into the lee of a mountain peak.  
579 Surface winds are modulated by a wide range of surface factors including trees, steep hills and hillocks,  
580 blocking by a steep slope, rolling hills, and structures (Supp. Fig S5). However, a combination of gusts  
581 (among thin wooded terrain on steep slopes) and the limited spatial extent of most obstacles underlies the  
582 agreement between the filtered AMOG and AJAX wind profiles. Agreement is better for the upper  
583 portions of the PBL (within 10-20%) where Sierra Nevada Mountain slopes are steeper. In contrast, the  
584 slope lower in the PBL is gentle, and surface boundary layer effects are more pronounced, biasing wind  
585 speeds slower.

586  
587 The wind orientation to the slope affects the comparison because topography imposes wind field structure  
588 at large and small scales. Where winds advect air upslope, transport incorporates a non-negligible vertical  
589 component that is missed by the 2D sonic anemometer used in the study reported here. The current  
590 AMOG configuration measures 3D winds, as does AJAX.

591  
592 Some of the discrepancy between AMOG and AJAX wind profiles could have arisen from temporal  
593 changes between the two profiles; however, this is unlikely for two reasons. First, the top of the PBL was

594 identified four times over the course of the study and remained stable within 100 m across the domain.  
595 And second, surface wind observations remained relatively constant after the mid-morning shift to  
596 daytime conditions (breakup of nocturnal stratification). However, the poor agreement between AJAX  
597 and AMOG vertical concentration profiles within the PBL suggests significant air mass shifts –  
598 highlighting the need for better concurrence.

#### 599 **4.4. GHG FFI emissions**

600 Emissions for the Kern Fields were estimated at  $32 \pm 16$  Gg  $\text{CH}_4 \text{ yr}^{-1}$  with  $\text{CH}_4$  emissions ~20% above  
601 EPA inventories, and  $2.4 \pm 1.2$  Tg  $\text{CO}_2 \text{ yr}^{-1}$ . The broad  $\text{CO}_2$  plume suggests emissions from the geologic  
602 reservoir – likely along the same pathways associated with  $\text{CH}_4$  leakage – in addition to the focused and  
603 not continuous emissions from the co-generation power plants. On China Loop Road (where the  $\text{CO}_2$   
604 surface plume was transected), strong crosswinds and light traffic would have prevented significant  
605 vehicular  $\text{CO}_2$  contamination. Additionally there are no upwind (non-oil field) roads, only the foothills of  
606 the Sierra Nevada Mountains.

607  
608 For comparison, a recent bottom-up estimate of  $\text{CH}_4$  emissions from the Kern Fields estimated  $25 \pm 15$  Gg  
609  $\text{CH}_4 \text{ yr}^{-1}$  by combining oil and gas production data with emissions factors for associated wells used by  
610 US-EPA (Jeong et al., 2014), i.e., 19 Aug. 2015  $\text{CH}_4$  emissions were a third above inventories. The  
611 derived flux lies within the inventory uncertainty, but is higher, consistent with a recent metastudy of  
612 field studies of FFI production emissions, which showed significant underestimation in the EPA budget  
613 (Brandt et al., 2014; Miller et al., 2013). A number of factors likely play a role including the age of the  
614 Kern River oil field (over a century), production factors (steam injection), shallowness of the reservoir  
615 (<300 m), location in a tectonically active area, which creates alternate migration pathways from the  
616 reservoir (Leifer et al., 2013), and the recent expansion of the number of wells in the Kern Front oil field  
617 (from GoogleEarth timeline imagery). Many of these factors are common to other production fields in  
618 California, the US, and globally. Given the importance of FFI to the overall budget, even small  
619 underestimation could be highly significant. Thus, this uncertainty highlights the need for improved  
620 measurement tools to reduce the significant uncertainty in the  $\text{CH}_4$  budget and for satellite measurement  
621 validation, particularly for complex terrain and in the source's near field..

#### 622 **5. Conclusion**

623 This study showed how to combine airborne and surface *in situ* data to improve emissions derivation, and  
624 demonstrated the novel use of topography to characterize vertical atmospheric structure with a surface

625 mobile platform. Given that mountains cover a significant fraction of the earth's land surface, further  
 626 research should be undertaken to confirm that this approach applies in other settings. Data showed the  
 627 PBL was not well-mixed, even 10-20 km downwind, highlighting the importance of the direct flux  
 628 quantification approach. Direct quantification does not require accurate modeling of winds across  
 629 complex terrain, but does require interpolation and data modeling to identify the background.

630

631 **Table of Nomenclature**

632		Units	Description
633	AJAX	(-)	Alpha Jet Atmospheric eXperiment
634	AMOG	(-)	AutoMOBILE trace Gas
635	Bbl	(-)	Barrel (of oil) 1 bbl = 6.38 m <sup>3</sup>
636	COMEX	(-)	CO <sub>2</sub> and METHANE eXperiment
637	EOR	(-)	Enhanced oil recovery (techniques)
638	EPA	(-)	Environmental Protection Agency
639	GCE	(-)	GOSAT COMEX Experiment
640	GHG	(-)	Greenhouse Gases
641	GOSAT	(-)	Greenhouse gases Observing SATellite
642	GHG	(-)	Greenhouse gas
643	PBL	(-)	Planetary Boundary Layer
644	SJV	(-)	San Joaquin Valley
645	Tg		Terragram (10 <sup>12</sup> g)
646	UTZ	(-)	Universal time
647	$C'(x,z)$	(ppm)	concentration anomaly (above $C_B$ )
648	$C(x,z)$	(ppm)	concentration
649	$C_B(x,z)$	(ppm)	background concentration – outside plume
650	$C_{BL}(z)$	(ppm)	background concentration profile – left side of profile
651	$C_{BR}(z)$	(ppm)	background concentration profile – right side of profile
652	$E$	(mol s <sup>-1</sup> )	Emission source strength
653	$k(z)$	(mol ppm <sup>-1</sup> )	Conversion factor from the ideal gas law
654	$N'$	(mol cm <sup>-3</sup> )	molar mass anomaly
655	$Q(x,z)$	(mol m <sup>-2</sup> s <sup>-1</sup> )	Flux through the data plane
656	$R^2$	(-)	Correlation coefficient
657	$RH$	(%)	Relative humidity
658	$T$	(°C)	Temperature

659	$U_n(x,z)$	(m s <sup>-1</sup> )	Winds normal to the data plane, a function of (x, z)
660	$U_{north}$	(m s <sup>-1</sup> )	North wind component
661	$U_{west}$	(m s <sup>-1</sup> )	West wind component
662	$x$	(m)	lateral distance – approximately cross-wind
663	$x_L$	(m)	left half of the transect ( $x < x_{max}/2$ )
664	$x_{max}$	(m)	length of a transect
665	$x_R$	(m)	right half of the transect ( $x > x_{max}/2$ )
666	$y$	(m)	lateral distance – approximately co-wind
667	$z$	(m)	altitude
668	$\Phi_L(C)$	(-)	concentration probability distribution for left side of transect
669	$\Phi_R(C)$	(-)	concentration probability distribution for right side of transect
670	$\Phi_P(C)$	(-)	concentration probability distribution for the plume
671	$\Phi_B(C)$	(-)	concentration probability distribution for the background
672	$\alpha, \alpha'$	(-)	designation for Delano – Alta Sierra surface transect
673	$\varepsilon, \varepsilon'$	(-)	designation for Edison– Breckenridge Mtn. surface transect
674	$\tau, \tau'$	(-)	designation for Breckenridge – Caliente surface transect
675	$\beta, \beta', \beta_1'$	(-)	designation for Wasco – Granite surface transect
676	$\gamma, \gamma'$	(-)	designation for Oildale – Oil City surface and airborne transects
677	$\delta, \delta'$	(-)	designation for Ming Park – Arvin surface and airborne transects

678

679 **Data Availability.** Data will be provided as per the data policy.

680

681 **Author Contribution.** I. Leifer prepared the manuscript with input from all co-authors. C. Melton  
682 prepared figures and conducted data analysis. M. Fischer helped prepare the emissions budgets. J. Frash  
683 helped with AMOG data collection. L. Iraci, J. Marrero, J-M. Ryoo, T. Tanaka, and E. Yates are part of  
684 the AJAX team and worked to collect and analyze AJAX data.

685 There are no competing interests

686

687 **Acknowledgements:** We thank the NASA Earth Science Division, Research and Analysis Program, grant  
688 NNX13AM21G. MLF was supported by a grant from the California Energy Commission's Natural  
689 Gas Research Program to the Lawrence Berkeley National Laboratory under contract DE-AC02-  
690 36605CH11231. AJAX data were collected under the AJAX project, which acknowledges the partnership  
691 of H211, LLC and support from the Ames Research Center Director's funds.

693 **6. References**

- 694 Allen, G.: Biogeochemistry: Rebalancing the global methane budget, *Nature*, 538, 46-48, 2016.
- 695 American Lung Association: State of the Air, 2016, American Lung Association, Chicago, IL,  
696 157 pp., 2016.
- 697 Bao, J. W., Michelson, S. A., Persson, P. O. G., Djalalova, I.V., and Wilczak, J. M.: Observed  
698 and WRF-simulated low-level winds in a high-ozone episode during the Central California  
699 Ozone Study, *Journal of Applied Meteorology and Climatology*, 47, 2372-2394, 2008.
- 700 Boucouvala, D. and Bornstein, R.: Analysis of transport patterns during an SCOS97-NARSTO  
701 episode, *Atmospheric Environment*, 37, Supplement 2, 73-94, 2003.
- 702 Brandt, A. R., Heath, G. A., Kort, E. A., O'Sullivan, F., Pétron, G., Jordaan, S. M., Tans, P.,  
703 Wilcox, J., Gopstein, A. M., Arent, D., Wofsy, S., Brown, N. J., Bradley, R., Stucky, G. D.,  
704 Eardley, D., and Harriss, R.: Methane leaks from North American natural gas systems,  
705 *Science*, 343, 733-735, 2014.
- 706 Calgem: California Greenhouse Gas Emissions Measurement (CALGEM) Project. DOE, 2014.
- 707 CARB: Facility GHG Emissions Visualization and Analysis Tool: 2008-2014. California  
708 Environmental Protection Agency, Air Resources Board, 2016.
- 709 Chen, H., Winderlich, J., Gerbig, C., Hofer, A., Rella, C. W., Crosson, E. R., Van Pelt, A. D.,  
710 Steinbach, J., Kolle, O., Beck, V., Daube, B. C., Gottlieb, E. W., Chow, V. Y., Santoni, G.  
711 W., and Wofsy, S. C.: High-accuracy continuous airborne measurements of greenhouse gases  
712 (CO<sub>2</sub> and CH<sub>4</sub>) using the cavity ring-down spectroscopy (CRDS) technique, *Atmos. Meas.*  
713 *Tech.*, 3, 375-386, 2010.
- 714 Dlugokencky, E. J., Crotwell, A., Masarie, K., White, J., Lang, P., and Crotwell, M.: NOAA  
715 Measurements of Long-lived Greenhouse Gases, *Asia-Pacific GAW Greenhouse Gases*, 6, 6-  
716 9, 2013.
- 717 Dlugokencky, E. J., Nisbet, E. G., Fisher, R., and Lowry, D.: Global atmospheric methane:  
718 Budget, changes and dangers, *Philosophical Transactions of the Royal Society A:*  
719 *Mathematical, Physical and Engineering Sciences*, 369, 2058-2072, 2011.
- 720 EPA: 2013 Inventory of US greenhouse gas: Emissions and sinks: 1990-2011, Environmental  
721 Protection Agency, Washington DC, 457 pp., 2013.
- 722 EPA: 2017 Inventory of US greenhouse gas: Emissions and sinks: 1990-2015, Environmental  
723 Protection Agency, Washington DC430-P-17-001, 633 pp., 2017.
- 724 European Commission: Emission Database for Global Atmospheric Research (EDGAR). Joint  
725 Research Centre (JRC)/Netherlands Environmental Assessment Agency (PBL), 2010.
- 726 Farrell, P., Leifer, I., and Culling, D.: Transcontinental methane measurements: Part 1. A mobile  
727 surface platform for source investigations, *Atmospheric Environment*, 74, 422-431, 2013.
- 728 Fernandez-Cortes, A., Cuezva, S., Alvarez-Gallego, M., Garcia-Anton, E., Pla, C., Benavente,  
729 D., Jurado, V., Saiz-Jimenez, C., and Sanchez-Moral, S.: Subterranean atmospheres may act  
730 as daily methane sinks, *Nature Communication*, 6, 2015.
- 731 Gentner, D. R., Ford, T. B., Guha, A., Boulanger, K., Brioude, J., Angevine, W. M., de Gouw, J.  
732 A., Warneke, C., Gilman, J. B., Ryerson, T. B., Peischl, J., Meinardi, S., Blake, D. R., Atlas,  
733 E., Lonneman, W. A., Kleindienst, T. E., Beaver, M. R., Clair, J. M. S., Wennberg, P. O.,  
734 VandenBoer, T. C., Markovic, M. Z., Murphy, J. G., Harley, R. A., and Goldstein, A. H.:



735 Emissions of organic carbon and methane from petroleum and dairy operations in  
736 California's San Joaquin Valley, *Atmospheric Chemistry and Physics*, 14, 4955-4978, 2014.

737 Ghosh, A., Patra, P. K., Ishijima, K., Umezawa, T., Ito, A., Etheridge, D. M., Sugawara, S.,  
738 Kawamura, K., Miller, J. B., Dlugokencky, E. J., Krummel, P. B., Fraser, P. J., Steele, L. P.,  
739 Langenfelds, R. L., Trudinger, C. M., White, J. W. C., Vaughn, B., Saeki, T., Aoki, S., and  
740 Nakazawa, T.: Variations in global methane sources and sinks during 1910–2010,  
741 *Atmospheric Chemistry and Physics*, 15, 2595-2612, 2015.

742 Hamill, P., Iraci, L. T., Yates, E. L., Gore, W., Bui, T. P., Tanaka, T., and Loewenstein, M.: A  
743 new instrumented airborne platform for atmospheric research, *Bulletin of the American*  
744 *Meteorological Society*, 97, 2015.

745 IPCC: *Climate Change 2007: Synthesis Report. Contribution of Working Groups I, II, and III to*  
746 *the Fourth Assessment Report of the Intergovernmental Panel on Climate Change*, IPCC,  
747 Geneva, Switzerland, 104 pp., 2007.

748 IPCC: *Working Group 1 Contribution to the IPCC Fifth Assessment Report Climate Change*  
749 *2013-The Physical Science Basis*, International Panel on Climate Change, IPCC Secretariat,  
750 Geneva, Switzerland, 2216 pp., 2013.

751 Jeong, S., Hsu, Y.-K., Andrews, A. E., Bianco, L., Vaca, P., Wilczak, J. M., and Fischer, M.:  
752 Multi-tower measurement network estimate of California's methane emissions, *Journal of*  
753 *Geophysical Research - Atmospheres*, 118, 2013JD019820, 2013.

754 Jeong, S., Zhao, C., Andrews, A. E., Bianco, L., Wilczak, J. M., and Fischer, M. L.: Seasonal  
755 variation of CH<sub>4</sub> emissions from central California, *Journal of Geophysical Research*, 117,  
756 2012.

757 Jeong, S. S., Millstein, D., and Fischer, M. L.: Spatially explicit methane emissions from  
758 petroleum production and the natural gas system in California, *Environmental Science &*  
759 *Technology*, 48, 5982-5990, 2014.

760 John, J. G., Fiore, A. M., Naik, V., Horowitz, L. W., and Dunne, J. P.: Climate versus emission  
761 drivers of methane lifetime against loss by tropospheric OH from 1860–2100, *Atmospheric*  
762 *Chemistry and Physics*, 12, 12021-12036, 2012.

763 Karion, A., Sweeney, C., Pétron, G., Frost, G., Michael Hardesty, R., Kofler, J., Miller, B. R.,  
764 Newberger, T., Wolter, S., Banta, R., Brewer, A., Dlugokencky, E., Lang, P., Montzka, S. A.,  
765 Schnell, R., Tans, P., Trainer, M., Zamora, R., and Conley, S.: Methane emissions estimate  
766 from airborne measurements over a western United States natural gas field, *Geophysical*  
767 *Research Letters*, 40, 4393-4397, 2013.

768 Karlsdóttir, S. and Isaksen, I. S. A.: Changing methane lifetime: Possible cause for reduced  
769 growth, *Geophysical Research Letters*, 27, 93-96, 2000.

770 Khalil, M. A. K. and Rasmussen, R. A.: *The changing composition of the Earth's atmosphere.*  
771 *In: Composition, chemistry, and climate of the atmosphere*, Singh, H. B. (Ed.), Van Nostrand  
772 Reinhold, New York, 1995.

773 Kirschke, S., Bousquet, P., Ciais, P., Saunoy, M., Canadell, J. G., Dlugokencky, E. J.,  
774 Bergamaschi, P., Bergmann, D., Blake, D. R., and Bruhwiler, L.: Three decades of global  
775 methane sources and sinks, *Nature Geoscience*, 6, 813-823, 2013.

776 Krautwurst, S., Gerilowski, K., Krings, T., Borchard, J., Bovensmann, H., Leifer, I., Fladland,  
777 M. M., Koyler, R., Iraci, L. T., Luna, B., Thompson, D. R., Eastwood, M., Green, R.,  
778 Jonsson, H. H., Vigil, S. A., and Tratt, D. M.: COMEX - Final Report: Scientific and  
779 Technical Assistance for the Deployment of a flexible airborne spectrometer system during  
780 CMAPEXP and COMEX, IUP-COMEX-FR, 148 pp., 2016.

781 Krings, T., Gerilowski, K., Buchwitz, M., Reuter, M., Tretner, A., Erzinger, J., Heinze, D.,  
782 Pflüger, U., Burrows, J. P., and Bovensmann, H.: MAMAP – a new spectrometer system for  
783 column-averaged methane and carbon dioxide observations from aircraft: Retrieval algorithm  
784 and first inversions for point source emission rates, *Atmospheric Measurement Techniques*,  
785 4, 1735-1758, 2011.

786 LaFranchi, B. W., Pétron, G., Miller, J. B., Lehman, S. J., Andrews, A. E., Dlugokencky, E. J.,  
787 Hall, B., Miller, B. R., Montzka, S. A., Neff, W., Novelli, P. C., Sweeney, C., Turnbull, J. C.,  
788 Wolfe, D. E., Tans, P. P., Gurney, K. R., and Guilderson, T. P.: Constraints on emissions of  
789 carbon monoxide, methane, and a suite of hydrocarbons in the Colorado Front Range using  
790 observations of  $^{14}\text{CO}_2$ , *Atmos. Chem. Phys.*, 13, 11101-11120, 2013.

791 Lamb, B. K., McManus, J., Shorter, J., Kolb, C., Mosher, B., Harriss, R., Allwine, E., Blaha, D.,  
792 Howard, T., Guenther, A., Lott, R., Siverson, R., Westburg, H., and Zimmerman, P.:  
793 Development of atmospheric tracer methods to measure methane emissions from natural gas  
794 facilities and urban areas, *Environmental Science & Technology*, 29, 1468-1479, 1995.

795 Leen, J. B., Yu, X. Y., Gupta, M., Baer, D. S., Hubbe, J. M., Kluzek, C. D., Tomlinson, J. M.,  
796 and Hubbell, M. R., 2nd: Fast in situ airborne measurement of ammonia using a mid-infrared  
797 off-axis ICOS spectrometer, *Environmental Science & Technology*, 47, 10446-10453, 2013.

798 Leifer, I., Culling, D., Schneising, O., Farrell, P., Buchwitz, M., and Burrows, J.:  
799 Transcontinental methane measurements: Part 2. Mobile surface investigation of fossil fuel  
800 industrial fugitive emissions, *Atmospheric Environment*, 74, 432-441, 2013.

801 Leifer, I., Melton, C., Frash, J., Fischer, M. L., Cui, X., Murray, J. J., and Green, D. S.: Fusion of  
802 mobile in situ and satellite remote sensing observations of chemical release emissions to  
803 improve disaster response, *Frontiers in Science*, 4, 1-14, 2016.

804 Leifer, I., Melton, C., Manish, G., and Leen, B.: Mobile monitoring of methane leakage, *Gases*  
805 *and Instrumentation*, July/August 2014, 20-24, 2014.

806 Lillis, P. G., Warden, A., Claypool, G. E., and Magoon, L. B.: Petroleum systems of the San  
807 Joaquin Basin Province -- geochemical characteristics of gas types: Chapter 10. In:  
808 Petroleum systems and geologic assessment of oil and gas in the San Joaquin Basin Province,  
809 California, Scheirer, A. H. (Ed.), 1713-10, U. S. Geological Survey, Reston, VA, 2008.

810 McKain, K., Down, A., Raciti, S. M., Budney, J., Hutyra, L. R., Floerchinger, C., Herndon, S.  
811 C., Nehrkorn, T., Zahniser, M. S., Jackson, R. B., Phillips, N., and Wofsy, S. C.: Methane  
812 emissions from natural gas infrastructure and use in the urban region of Boston,  
813 Massachusetts, *Proceedings of the National Academy of Sciences*, 2015. 2015.

814 Miller, S. M., Wofsy, S. C., Michalak, A. M., Kort, E. A., Andrews, A. E., Biraud, S. C.,  
815 Dlugokencky, E. J., Eluszkiewicz, J., Fischer, M. L., Janssens-Maenhout, G., Miller, B. R.,  
816 Miller, J. B., Montzka, S. A., Nehrkorn, T., and Sweeney, C.: Anthropogenic emissions of  
817 methane in the United States, *Proceedings of the National Academy of Sciences*, 110, 20018-  
818 20022, 2013.

819 NASA: <https://www.nasa.gov/image-feature/goddard/wildfires-in-california-august-17-2015>, last  
820 access: 16 April 2017, 2015.

821 Nisbet, E. G., Dlugokencky, E. J., and Bousquet, P.: Methane on the rise—Again, *Science*, 343,  
822 493-495, 2014.

823 Nisbet, E. G., Dlugokencky, E. J., Manning, M. R., Lowry, D., Fisher, R. E., France, J. L.,  
824 Michel, S. E., Miller, J. B., White, J. W. C., Vaughn, B., Bousquet, P., Pyle, J. A., Warwick,  
825 N. J., Cain, M., Brownlow, R., Zazzeri, G., Lanoisellé, M., Manning, A. C., Gloor, E.,  
826 Worthy, D. E. J., Brunke, E. G., Labuschagne, C., Wolff, E. W., and Ganesan, A. L.: Rising

827 atmospheric methane: 2007–2014 growth and isotopic shift, *Global Biogeochemical Cycles*,  
828 30, 1356-1370, 2016.

829 Peischl, J., Karion, A., Sweeney, C., Kort, E. A., Smith, M., L., Brandt, A. R., Yeskoo, T.,  
830 Aikin, K. C., Conley, S. A., and Gvakharia, A.: Quantifying atmospheric methane emissions  
831 from oil and natural gas production in the Bakken shale region of North Dakota, *Journal of*  
832 *Geophysical Research: Atmospheres*, 212, 2016.

833 Peischl, J., Ryerson, T. B., Aikin, K. C., de Gouw, J. A., Gilman, J. B., Holloway, J. S., Lerner,  
834 B. M., Nadkarni, R., Neuman, J. A., Nowak, J. B., Trainer, M., Warneke, C., and Parrish, D.  
835 D.: Quantifying atmospheric methane emissions from the Haynesville, Fayetteville, and  
836 northeastern Marcellus shale gas production regions, *Journal of Geophysical Research:*  
837 *Atmospheres*, 120, 2119-2139, 2015.

838 Peischl, J., Ryerson, T. B., Brioude, J., Aikin, K. C., Andrews, A. E., Atlas, E., Blake, D., Daube,  
839 B. C., de Gouw, J. A., Dlugokencky, E., Frost, G. J., Gentner, D. R., Gilman, J. B.,  
840 Goldstein, A. H., Harley, R. A., Holloway, J. S., Kofler, J., Kuster, W. C., Lang, P. M.,  
841 Novelli, P. C., Santoni, G. W., Trainer, M., Wofsy, S. C., and Parrish, D. D.: Quantifying  
842 sources of methane using light alkanes in the Los Angeles basin, California, *Journal of*  
843 *Geophysical Research: Atmospheres*, 118, n/a-n/a, 2013.

844 Pétron, G., Frost, G., Miller, B. R., Hirsch, A. I., Montzka, S. A., Karion, A., Trainer, M.,  
845 Sweeney, C., Andrews, A. E., Miller, L., Kofler, J., Bar-Ilan, A., Dlugokencky, E. J., Patrick,  
846 L., Moore, C. T. J., Ryerson, T. B., Siso, C., Kolodzey, W., Lang, P. M., Conway, T.,  
847 Novelli, P., Masarie, K., Hall, B., Guenther, D., Kitzis, D., Miller, J., Welsh, D., Wolfe, D.,  
848 Neff, W., and Tans, P.: Hydrocarbon emissions characterization in the Colorado Front  
849 Range: A pilot study, *J. Geophys. Res.*, 117, D04304, 2012.

850 Rigby, M., Montzka, S. A., Prinn, R. G., White, J. W. C., Young, D., O'Doherty, S., Lunt, M. F.,  
851 Ganesan, A. L., Manning, A. J., Simmonds, P. G., Salameh, P. K., Harth, C. M., Mühle, J.,  
852 Weiss, R. F., Fraser, P. J., Steele, L. P., Krummel, P. B., McCulloch, A., and Park, S.: Role  
853 of atmospheric oxidation in recent methane growth, *Proceedings of the National Academy of*  
854 *Sciences*, 114, 5373-5377, 2017.

855 Rigby, M., Prinn, R. G., Fraser, P. J., Simmonds, P. G., Langenfelds, R. L., Huang, J., Cunnold,  
856 D. M., Steele, L. P., Krummel, P. B., Weiss, R. F., O'Doherty, S., Salameh, P. K., Wang, H.  
857 J., Harth, C. M., Mühle, J., and Porter, L. W.: Renewed growth of atmospheric methane,  
858 *Geophys. Res. Lett.*, 35, L22805, 2008.

859 Saunio, M., Bousquet, P., Poulter, B., Peregón, A., Ciais, P., Canadell, J. G., Dlugokencky, E.  
860 J., Etiope, G., Bastviken, D., Houweling, S., Janssens-Maenhout, G., Tubiello, F. N.,  
861 Castaldi, S., Jackson, R. B., Alexe, M., Arora, V. K., Beerling, D. J., Bergamaschi, P., Blake,  
862 D. R., Brailsford, G., Brovkin, V., Bruhwiler, L., Crevoisier, C., Crill, P., Curry, C.,  
863 Frankenberg, C., Gedney, N., Höglund-Isaksson, L., Ishizawa, M., Ito, A., Joos, F., Kim, H.  
864 S., Kleinen, T., Krummel, P., Lamarque, J. F., Langenfelds, R., Locatelli, R., Machida, T.,  
865 Maksyutov, S., McDonald, K. C., Marshall, J., Melton, J. R., Morino, I., O'Doherty, S.,  
866 Parmentier, F. J. W., Patra, P. K., Peng, C., Peng, S., Peters, G. P., Pison, I., Prigent, C.,  
867 Prinn, R., Ramonet, M., Riley, W. J., Saito, M., Schroeder, R., Simpson, I. J., Spahni, R.,  
868 Steele, P., Takizawa, A., Thornton, B. F., Tian, H., Tohjima, Y., Viovy, N., Voulgarakis, A.,  
869 van Weele, M., van der Werf, G., Weiss, R., Wiedinmyer, C., Wilton, D. J., Wiltshire, A.,  
870 Worthy, D., Wunch, D. B., Xu, X., Yoshida, Y., Zhang, B., Zhang, Z., and Zhu, Q.: The  
871 global methane budget: 2000-2012, *Earth System Science Data Discussion*, 2016, 1-79,  
872 2016.

873 Saunois, M., Bousquet, P., Poulter, B., Peregon, A., Ciais, P., Canadell, J. G., Dlugokencky, E.  
874 J., Etiope, G., Bastviken, D., Houweling, S., Janssens-Maenhout, G., Tubiello, F. N.,  
875 Castaldi, S., Jackson, R. B., Alexe, M., Arora, V. K., Beerling, D. J., Bergamaschi, P., Blake,  
876 D. R., Brailsford, G., Bruhwiler, L., Crevoisier, C., Crill, P., Covey, K., Frankenberg, C.,  
877 Gedney, N., Höglund-Isaksson, L., Ishizawa, M., Ito, A., Joos, F., Kim, H.-S., Kleinen, T.,  
878 Krummel, P., Lamarque, J. F., Langenfelds, R., Locatelli, R., Machida, T., Maksyutov, S.,  
879 Melton, J. R., Morino, I., Naik, V., O'Doherty, S., Parmentier, F. J. W., Patra, P. K., Peng, C.,  
880 Peng, S., Peters, G. P., Pison, I., Prinn, R., Ramonet, M., Riley, W. J., Saito, M., Santini, M.,  
881 Schroeder, R., Simpson, I. J., Spahni, R., Takizawa, A., Thornton, B. F., Tian, H., Tohjima,  
882 Y., Viovy, N., Voulgarakis, A., Weiss, R., Wilton, D. J., Wiltshire, A., Worthy, D., Wunch,  
883 D., Xu, X., Yoshida, Y., Zhang, B., Zhang, Z., and Zhu, Q.: Variability and quasi-decadal  
884 changes in the methane budget over the period 2000–2012, *Atmosphere Chemistry and*  
885 *Physics*, 17, 11135-11161, 2017.

886 Schwietzke, S., Sherwood, O. A., Bruhwiler, L. M. P., Miller, J. B., Etiope, G., Dlugokencky, E.  
887 J., Michel, S. E., Arling, V. A., Vaughn, B. H., White, J. W. C., and Tans, P. P.: Upward  
888 revision of global fossil fuel methane emissions based on isotope database, *Nature*, 538, 88-  
889 91, 2016.

890 Simpson, I. J., Sulbaek Andersen, M. P., Meinardi, S., Bruhwiler, L., Blake, N. J., Helmig, D.,  
891 Rowland, F. S., and Blake, D. R.: Long-term decline of global atmospheric ethane  
892 concentrations and implications for methane, *Nature*, 488, 490-494, 2012.

893 Smith, M. L., Kort, E. A., Karion, A., Sweeney, C., Herndon, S. C., and Yacovitch, T. I.:  
894 Airborne ethane observations in the Barnett Shale: Quantification of ethane flux and  
895 attribution of methane emissions, *Environmental Science & Technology*, 49, 8158-8166,  
896 2015.

897 Sonnemann, G. R. and Grygalashvily, M.: Global annual methane emission rate derived from its  
898 current atmospheric mixing ratio and estimated lifetime, *Annales Geophysicae*, 32, 277-283,  
899 2014.

900 Sun, K., Tao, L., Miller, D. J., Khan, A. M., and Zondlo, M. A.: On-road ammonia emissions  
901 characterized by mobile, open-path measurements, *Environmental Science & Technology*,  
902 48, 3943-3950, 2014.

903 Tanaka, T., Yates, E., Iraci, L. T., Johnson, M. S., Gore, W., Tadi, J. M., Loewenstein, M., Kuze,  
904 A., Frankenberg, C., Butz, A., and Yoshida, Y.: Two-year comparison of airborne  
905 measurements of CO<sub>2</sub> and CH<sub>4</sub> with GOSAT at Railroad Valley,  
906 Nevada, *IEEE Transactions on Geoscience and Remote Sensing*, 54, 4367-4375, 2016.

907 Thompson, D., Leifer, I., Bovensman, H., Eastwood, M., Fladland, M., Frankenberg, C.,  
908 Gerilowski, K., Green, R., Krautwurst, S., Krings, T., Luna, B., and Thorpe, A. K.: Real-time  
909 remote detection and measurement for airborne imaging spectroscopy: A case study with  
910 methane, *Atmospheric Measurement Techniques*, 8, 1-46, 2015.

911 VanCuren, R.: Transport aloft drives peak ozone in the Mojave Desert, *Atmospheric*  
912 *Environment*, 109, 331-341, 2015.

913 Wennberg, P. O., Mui, W., Wunch, D., Kort, E. A., Blake, D. R., Atlas, E. L., Santoni, G. W.,  
914 Wofsy, S. C., Diskin, G. S., Jeong, S., and Fischer, M. L.: On the sources of methane to the  
915 Los Angeles atmosphere, *Environmental Science & Technology*, 46, 9282-9289, 2012.

916 White, W. H., Anderson, J. A., Blumenthal, D. L., Husar, R. B., Gillani, N. V., Husar, J. D., and  
917 Wilson, W. E.: Formation and transport of secondary air pollutants: Ozone and aerosols in  
918 the St. Louis urban plume, *Science*, 194, 187-189, 1976.

919 Wunch, D., Wennberg, P. O., Toon, G. C., Keppel-Aleks, G., and Yavin, Y. G.: Emissions of  
920 greenhouse gases from a North American megacity, *Geophysical Research Letters.*, 36, 2009.  
921 Yacovitch, T. I., Herndon, S. C., Pétron, G., Kofler, J., Lyon, D., Zahniser, M. S., and Kolb, C.  
922 E.: Mobile laboratory observations of methane emissions in the Barnett Shale Region,  
923 *Environmental Science & Technology*, 49, 7889-7895, 2015.  
924 Yates, E. L., Iraci, L. T., Roby, M. C., Pierce, R. B., Johnson, M. S., Reddy, P. J., Tadić, J. M.,  
925 Loewenstein, M., and Gore, W.: Airborne observations and modeling of springtime  
926 stratosphere-to-troposphere transport over California, *Atmospheric Chemistry Physics*, 13,  
927 12481-12494, 2013.  
928 Zhong, S., Whiteman, C. D., and Bian, X.: Diurnal evolution of three-dimensional wind and  
929 temperature structure in California's Central Valley, *Journal of Applied Meteorology*, 43,  
930 1679-1699, 2004.  
931